COMBUSTION CHARACTERISTICS OF A TWO-STROKE LARGE BORE NATURAL GAS SPARK-IGNITED ENGINE

A Thesis

by

AARON ALEXANDER GRIFFIN

Submitted to the Office of Graduate and Professional Studies of
Texas A&M University
in partial fulfillment of the requirements for the degree of

MASTER OF SCIENCE

Chair of Committee,	Timothy J. Jacobs
Committee Members,	Jerald A. Caton
	Terry Creasy
Head of Department,	Andreas Polycarpou

August 2015

Major Subject: Mechanical Engineering

ABSTRACT

Naturally, there are complex interactions among internal combustion engine parameters such as in-cylinder pressure, emissions, speed, and load. These basic relationships are studied in a naturally aspirated, spark-ignited, two-stroke, large-bore natural gas engine. The typical application for such an engine is operating heavy machinery such as large compressors and oil field pump jacks.

Cylinder pressure averaged over 300 cycles is captured for eight speeds from 350 to 525 RPM and six loads of 50% to 100% of maximum torque at each respective speed. Non-sequential individual cycle pressure curves are captured to depict cyclic variation at each operating point. Emissions are measured for each operating point. Equivalence ratio, delivery ratio, and trapping efficiencies are also calculated. The behavior of these parameters are then quantified and described in the context of cyclic variation.

It is shown that low load cyclic variation is extreme, having coefficient of variance (COV) of indicated mean effective pressure (IMEP) values over 40%. Low load cycles are shown to frequently misfire or experience partial burn. Cyclic variation is shown to decrease with increasing load and decreasing speed. Air flow rate is shown to increase with engine speed. It is also shown that the overall system equivalence ratio is highest at high loads and low speeds, and the values are between 0.55 and 0.90. Brake specific fuel consumption (BSFC) is suspected to decrease with increasing load, likely due to improved scavenging at high load. Delivery ratio is shown to be, on average, slightly greater than 1.0 at most operating conditions.

Fuel trapping efficiency has a complex trend with increasing speed. Air trapping efficiencies disagree with those calculated for fuel, and are likely incorrect due to the lean-burning nature of the engine. Scavenging efficiency results are not credible. Emissions of CO_2, NO, and THC are shown (and emissions of CH_4 are suspected) to have an inverse correlation with cyclic variation; emissions of O_2 are shown (and emissions of CO are suspected) to have direct correlation with cyclic variation.

DEDICATION

To my future wife, Holly, and all the Griffin family

ACKNOWLEDGEMENTS

I am greatly indebted to my friends and coworkers, past and present, in the laboratory. From providing a friendly smile every day to assisting in solving rigorous and complex issues, I can't thank each of them enough. They have been such an enormous part of why I have so sincerely enjoyed my time in the lab. I am particularly grateful for Alireza Mashayekh and Abdullah Bajwa for their assistance in the experimentation phase of the project.

I would like to acknowledge GE Oil & Gas for its financial, hardware, and technical support. I am particularly thankful for the contributions of Ken Ashraph, Gerardo Mendez, John Etcheverry, and Drake Pate.

I would like to thank my committee chair, Dr. Tim Jacobs, for all of his patience and wisdom. He was a beacon of academic light throughout the course of the project, illuminating the way forwards on countless occasions. He always had confidence that I could accomplish whatever was necessary, even when I myself had no such confidence. I would also like to thank my committee members, Dr. Caton and Dr. Creasy, for their time and support in this project.

I am forever grateful for and indebted to my amazing family. The value of a great education was something my parents constantly emphasized to me from a very early age; I am humbled to have been given such a grand opportunity. I am also so thankful for my older brother, Adam, who gave me great footsteps to follow.

I am so thankful for my fiancée, Holly. Her patience, kindness, and grace have given me the liberty to pursue completion of this project; her love has been my motivation throughout. She is my best friend and has been so much more helpful than she will ever know. I am so excited to marry her!

Above all, however, I am thankful for Jesus Christ. Ephesians chapter two says, and rightly so, that I was dead in my sins, but God made me alive in Jesus Christ. His sacrifice has given me life; by his stripes I am healed. I was powerless to obey the law of God; Jesus fulfilled the law, and now he is my righteousness. Faith in his life, death, and resurrection has given me new life, new joy, and a new family. Praise be to Jesus Christ, the Savior of the world, the hope of mankind, and glory be to God forever for what Jesus has done. It is finished!

NOMENCLATURE

°ATDC	Degrees of Crank Angle After Top Dead Center
°CA	Degrees of Crank-Angle
“w.c.	Inches of Water Column
AFR	Air-to-Fuel Ratio
BDC	Bottom Dead Center
bhp	Brake Horsepower
BSFC	Brake Specific Fuel Consumption
bsNO	Brake Specific Emissions of Nitric Oxide
BTDC	Before Top Dead Center
cDAQ	Compact Data Acquisition
CFD	Computational Fluid Dynamics
CO	Carbon Monoxide
CO_2	Carbon Dioxide
COV	Coefficient of Variance
cRIO	Compact Reconfigurable Input/Output
DAQ	Data Acquisition
EGR	Exhaust Gas Recirculation
EPC	Exhaust Port Close
EPO	Exhaust Port Open
GM	General Motors

HC	Hydrocarbons
HCN	Hydrogen Cyanide
IC	Internal Combustion
IMEP	Indicated Mean Effective Pressure
NI	National Instruments
NO	Nitric Oxide
NO_x	Oxides of Nitrogen
O_2	Diatomic Oxygen
ppm	Parts Per Million
ppr	Pulses Per Revolution
RPM	Revolutions Per Minute
SCFM	Standard Cubic Feet Per Minute
SI	Spark-Ignited
TDC	Top Dead Center
V	Volts

TABLE OF CONTENTS

Page

LIST OF FIGURES

Page

LIST OF TABLES

Page

1. INTRODUCTION

1.1. Motivation

Engine manufacturers are mandated to meet legislated regulations governing engine emissions. Often, dated engine designs require reexamination to maintain compliance or offer novel and improved engines. The present study investigates a "legacy" natural gas, two-stroke, large-bore engine that is prolific in the oil and gas industry and offers opportunities to improve industry emissions and efficiency.

The design of this engine dates to the 1960s, prior to proliferation of model- and simulation-based design. At such a time, design criteria centered on reliability and performance. Presently, in addition to reliability and performance, engine emissions and efficiency also serve as design criteria. This study sets the stage for continued and modern engine development of a robust and prolific engine platform.

1.2. Background

1.2.1. Two-Stroke Cycle

The two stroke cycle uses only one revolution, or two piston strokes, to accomplish the compression, expansion, exhaust, and intake processes. During combustion, the piston travels towards bottom dead center (BDC) due to the expanding gasses. Meanwhile, the retreating piston is compressing the fuel-and-air mixture in the stuffing box, which is contained by a reed valve (i.e., a check valve on the fuel and air supply ports). As the piston travels past the exhaust port, the combustion products exit through the exhaust manifold in a process called blowdown. The piston continues traveling towards BDC, uncovering the intake port. Because of the higher pressure in

the stuffing box compared to that of the combustion chamber, a fresh charge of fuel and air is pushed from the stuffing box into the combustion chamber. The piston reaches BDC, and then reverses direction, traveling towards top dead center (TDC). The intake port is covered, then the exhaust port. This traps the gasses inside the cylinder, and compression begins. As the piston nears TDC, the spark fires initiating combustion and allowing the cycle to repeat.

1.2.2. Scavenging

One unique feature of many two stroke cycles is that the intake event completely overlaps the exhaust event, occurring simultaneously for approximately 100°CA in a process called scavenging. In a cross-head scavenged engine, when both the intake and exhaust ports are uncovered by the piston, the fresh charge for the upcoming combustion event travels in a loop within the combustion chamber, mixing with and displacing the exhaust gasses from the previous combustion event. Some of the fresh charge, however, can and does travel directly from the intake port across the diameter of the cylinder to the exhaust port; this is known as short-circuiting. Since short-circuiting passes fuel directly into the exhaust stream, specific fuel consumption and HC emissions of such engine designs are higher [1] than other two-stroke or four-stroke designs.

Thus, two stroke engines, though more reliable and durable due to fewer moving parts such as valves and cams, are not without their disadvantages. Reliability, however, is critical in the pipeline industry. These engines must operate continuously throughout the year to maximize return on investment; the feature of fewer moving parts in a two stroke cycle greatly assists these engines in achieving that objective.

Internal combustion (IC) engines, particularly two-stroke engines, are prone to cyclic variation, also known as cyclic dispersion. Cyclic variation is the cycle-to-cycle difference in measured or calculated values related to combustion performance, namely the in-cylinder pressure as a function of engine crank angle. The combustion behavior impacts nearly all other engine parameters. In-cylinder temperature is much lower during misfiring cycles, which significantly changes emission characteristics. Misfiring due to cyclic variation increases THC emissions, since the entire fresh charge of natural gas exits into the exhaust stream. These are only a few examples of how cyclic variation can affect other parameters, which sets the stage for this study.

1.3. Objective

The objective of this study, resulting from the recently commissioned installation of the engine under study, is to quantify the behavior and describe within the context of cyclic variation the following engine parameters as functions of speed and load: in-cylinder pressure, coefficient of variance (COV) of indicated mean effective pressure (IMEP), air flow rate, equivalence ratio, delivery ratio, air and fuel trapping efficiencies, and emissions such as carbon monoxide (CO), carbon dioxide (CO_2), oxygen (O_2), nitric oxide (NO), total hydrocarbons (THC), and methane (CH_4).

2. LITERATURE REVIEW

2.1. Cyclic Variation

It has been found that the culprit for such variability is the time required for the flame kernel to transition into a developed flame front [2-4]. Since this transition occurs using such a small fraction of the combustion chamber volume, factors local to the spark plug are far more dominant than global averages within the cylinder [2, 5, 6]. For an example of the size of this region, the critical radius around the spark plug in the engine used in the study conducted by Winsor and Patterson is 10.2 mm (0.4 in) [5]. For reference, the engine used in that study has a bore of 82.6 mm (3.25 in) and a stroke of 114.2 mm (4.5 in).

Factors influencing this site include poor scavenging near the spark plug [2], as well as the velocity and turbulence of the fluid surrounding the spark event [5, 7, 8]; turbulence increases with increasing speed [9, 10], inhibiting a quick transition from flame kernel to developed flame front.

Another factor influencing the development of the flame kernel is the local air-fuel ratio near the spark plug [9, 11]. At low load, the rate of mass fraction burned is noticeably slower than at higher load. Though the effect of a significant residual fraction causes a slightly lower flame speed [6], the slower burn rate is primarily a result of the delayed development of the flame kernel [9, 11].

An additional factor that influences the growth of the flame kernel is poor mixing of the fresh charge and lingering exhaust products [9, 11]. Higher speeds intensify this issue [9, 10] which results in an increase of misfires or partial burn events, where a

kernel is successfully formed but the flame cannot propagate through the entire cylinder [12].

One global factor that has been shown to have reasonable impact on the rate of mass fraction burned is the global equivalence ratio [13]. This has little impact on the transition from flame kernel to a developed flame front but has significant impact on the flame speed after flame front development. Mixtures having an equivalence ratio closer to stoichiometric typically have a higher flame speed, and thus are less prone to cyclic variations.

2.2. Effects of Engine Speed

Engine speed and load are key parameters of interest in this study. For example, a study performed by Mavropoulos et al. [14, 15] shows that heat transfer coefficients for heat transfer out of the cylinder increase with speed, irrespective of load. This is likely due to the increased swirl and turbulence within the cylinder. Gas velocities are higher at higher engine speeds due to the higher mean piston speed.

Exhaust temperatures [14] and mass-averaged in-cylinder temperatures [16] were found to increase with engine speed. This has a differing effect on emissions. On one hand, higher temperatures reduce total THC emissions, and higher engine speeds reduce the residence time, which inhibits NO formation. On the other hand, increased temperatures with increased engine speed promote production of NO [15]. Heywood et al. [17], however, demonstrates that as speed increases at a given load, predicted NO formation increases. These two studies conclude differently regarding the trend of NO

production with respect to increasing engine speed. This could indicate that the effect of speed depends on the engine geometry and configuration.

Sawada et al. found that THC, CO, and NO emissions decrease with increasing engine speed [18], from 5,000 RPM to 8,000 RPM. The trend for THC production agrees with a study conducted by Duret et al. [19]. However, because of the high engine speeds, the trends of Sawada's and Duret's experiments may not translate to the slower speeds of the engine used in this study.

Engine speed also affects specific fuel consumption. Found in Heywood's study is a predicted slight decrease in specific fuel consumption with increasing speed at a constant load [17] shown in Figure 1. Heywood's finding agrees with a conclusion from Abthoff at al., studied on a portloop scavenged engine [20]. A study on a two-stroke engine performed by Nomura and Nakamura, however, shows specific fuel consumption at wide-open throttle increases as engine speed increases [21].

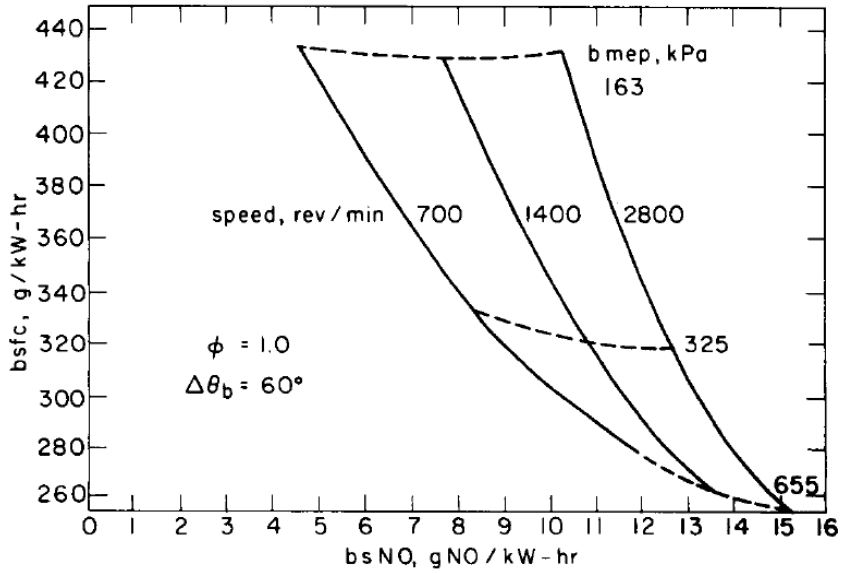

Figure 1. Brake specific fuel consumption and brake specific NO production rate are shown as functions of engine speed and load [17].

2.3. Effects of Engine Load

Performance parameters in an engine are influenced by engine load. For example, increasing engine load increases the exhaust temperature [17, 22]. As mentioned previously, this can help reduce HC emissions; CO emissions, however, trend increasingly [23]. These effects are shown in Figure 2. The increasing exhaust temperatures seem to be indicative of increasing reaction temperatures, too, as NO emission can be promoted. This trend, however, is speculative.

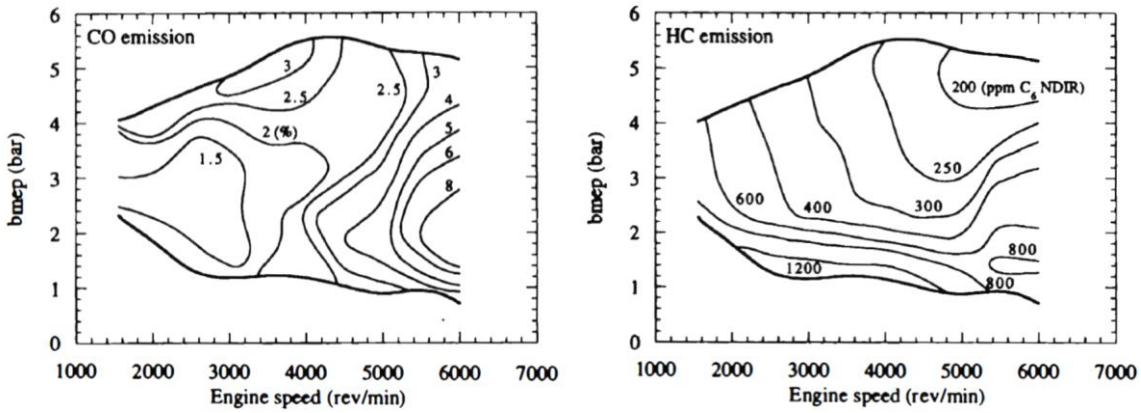

(A) (B)

Figure 2. Emissions from a two-stroke SI scooter engine: (A). CO in volumetric percent. (B). HC in ppm [23].

Engine load also has a strong influence on brake power and efficiency. Typically, for the majority of the operating envelope of an engine, a higher load requires a lower specific fuel consumption and, therefore, has a higher thermal efficiency; an example of this is shown in Figure 3. These results agree with those found in Figure 1.

Future work could be performed in a deeper review of literature specific to two-stroke engines. Many papers published near the time period surrounding the design and development of engines similar to that used in this study are likely to include valuable information. Papers specifically from the 1950s-1970s should be considered.

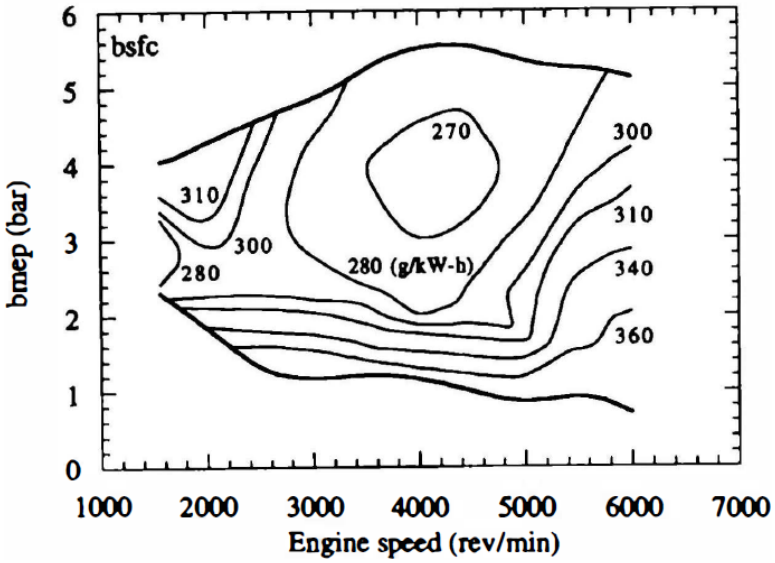

Figure 3. Specific fuel consumption from a two-stroke SI scooter engine [23].

2.4. Expectations from Literature

From the literature review, several trends seem likely to be encountered in this study. Since increasing speed increases turbulence which discourages flame kernel growth, cyclic variation should increase with increasing speed. Additionally, since the engine is designed to scavenge properly at full load, cyclic variation should decrease with increasing load.

THC emissions levels should decrease with increasing speed and increasing load. CO emissions should decrease with increasing speed and increase with increasing load. BSFC should decrease with increasing load. These expectations will be compared to the results of this study.

Several other trends, however, might depend on characteristics specific to the engine in study. Results for the response of NO emissions to speed and load are not

definitive. Neither is the response of BSFC to a change in speed. These will be determined for the engine used in this study.

3. EXPERIMENTAL SET-UP

In order to adequately understand results from an experiment, it is important to know details about the engine, instrumentation, and DAQ. Also, the test matrix is the grid of operating conditions by which it is experimentally determined how speed and load change engine parameters. How these parameters are calculated and any assumptions made in the experiment are also important.

3.1. Equipment

3.1.1. Engine

The presented study is conducted experimentally on a newly commissioned large-bore natural gas engine. The engine specifications are thus: single cylinder, 2-stroke, 9.3L displacement, naturally-aspirated, spark-ignited, and natural gas fueled. Such an engine is commonly used in the oil and gas industry for stationary power applications (e.g., operating an oil field pump jack). Table 1 lists the important characteristics of the engine. Since the engine is quite new, future work should be conducted to determine, if necessary, a break-in procedure for the engine to ensure optimal performance.

Table 1. Specifications of the single cylinder engine used in this study.

Property	SI Units		Imperial Units	
Bore	216	mm	8.5	in
Stroke	254	mm	10	in
Displacement	9.3	L	567	in^3
Compression Ratio	6:1	--	--	--
Rated Continuous Power	29.8	kW	40	Bhp
Rated Speed	525	RPM	--	--
Rated Max. Continuous Torque	540	N-m	400	ft-lbf
Engine Weight	2000	kg	4420	lbf
Flywheel Weight	680	kg	1500	lbf

A cross sectional view of the engine can be seen in Figure 4. Air and fuel (natural gas) enter the intake manifold on top of the engine. These must pass through a reed valve which requires a pressure differential between the manifold and the stuffing box. As the piston travels towards TDC, the pressure differential is achieved, and the reed valve opens to allow flow into the stuffing box.

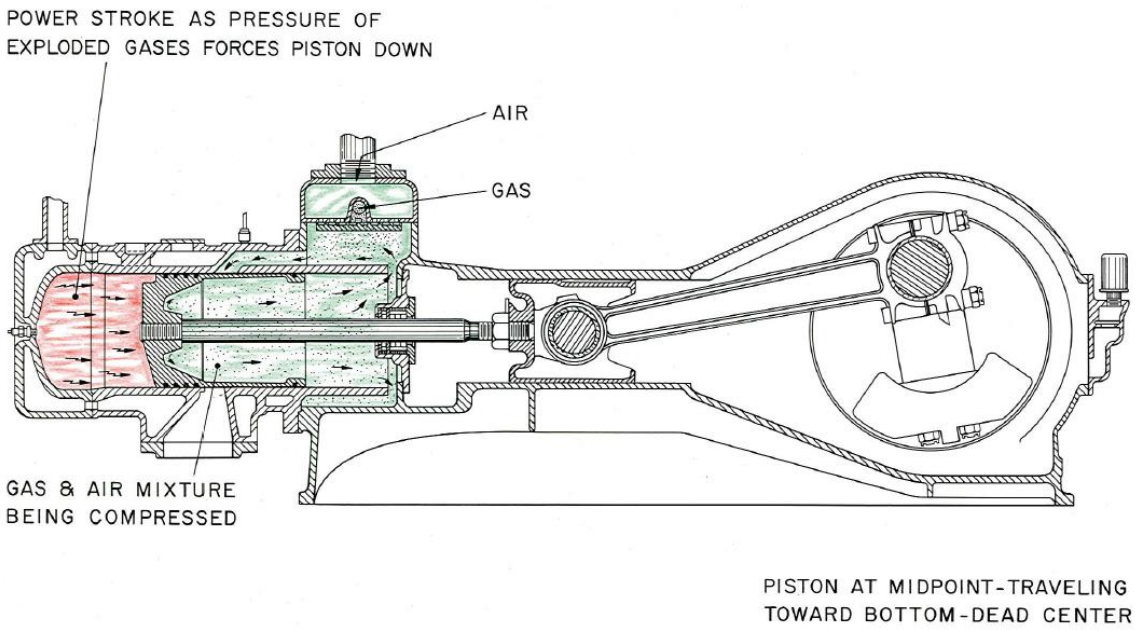

Figure 4. Cross-sectional view of engine, where red denotes combusting gasses and green denotes a fuel-and-air mixture [24].

As the intake port is uncovered, the combustion chamber is cross-scavenged. The details of this are shown in Figure 5. The engine is supplied with natural gas from the city of College Station. It enters the facility at approximately 10 psig and passes through a regulator by which it is reduced to approximately 10”w.c. The composition of the natural gas, as determined on March 3, 2015, is shown in Table 2.

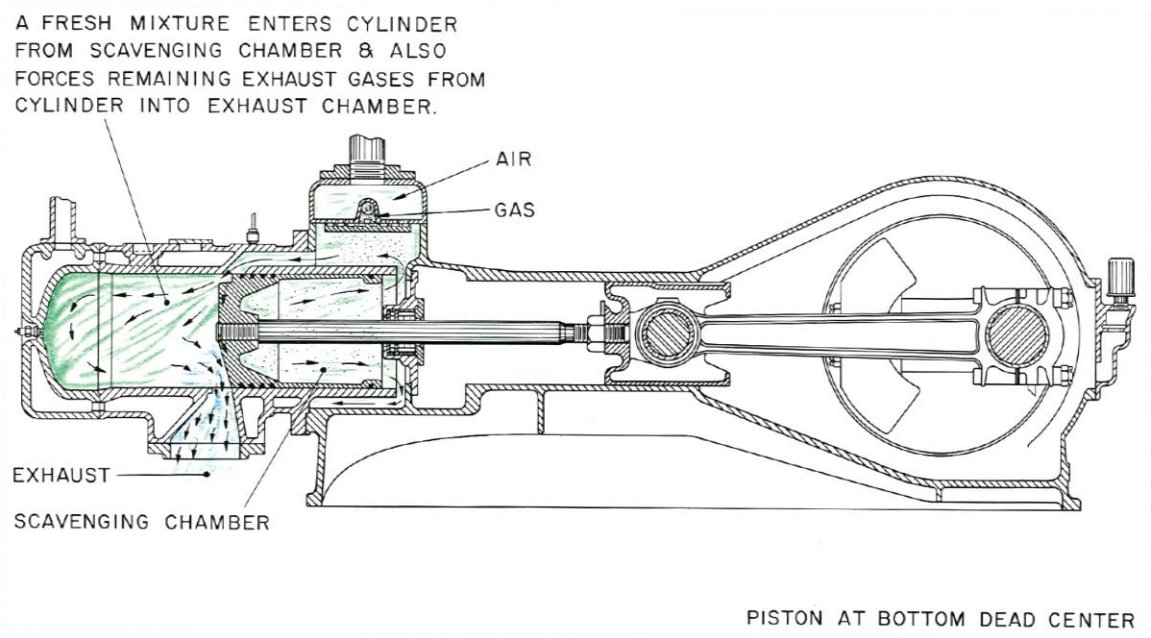

Figure 5. Cross-sectional view of engine, where blue denotes exhaust gasses [24].

Table 2. College Station natural gas composition, as determined on March 3, 2015 [25].

Constituent	Fraction (mol %)
Methane	92.57
Ethane	4.39
Propane	0.24
Butane	0.05
Pentane	0.04
Hexane	0.02
Carbon Dioxide	1.10
Nitrogen	1.59

The spark to initiate combustion is triggered by a magnet on the flywheel. As the magnet passes through a sensor, which is rigidly mounted to the body of the engine, the sensor detects the magnetic flux and sends a signal to the spark to fire. Since the magnet

and the sensor are rigidly mounted, the spark timing cannot be changed during testing. Spark occurs at 11.2°BTDC.

3.1.2. Dynamometer

Connected to the engine is a 50 kW, air cooled, eddy current dynamometer, which applies and measures load on the engine. A control signal of 0-10 VDC is regulated by a potentiometer and sent to the dynamometer to command load. This voltage regulates the amount of electrical current sent through the windings on the stator. The amount of current modifies the strength of the magnetic field generated. The rotor rotates through this magnetic field, producing an electromagnetic force and thus creating back, or resistive, work [26]. The energy from the engine is dissipated into the ambient air as thermal energy.

The dynamometer is equipped with a load cell. As the stator provides torque on the rotor, the entire stator-rotor assembly, forming a lever arm, pivots about a shaft on bearings. At the end of the lever arm is a load cell, which is secured to the chassis of the dynamometer. The load cell outputs a voltage proportional to the force it exerts to maintain the assembly's position, which is geometrically proportional to the torque that the stator is exerting on the rotor. The voltage is measured using a multimeter, and a linear calibration function is applied to the voltage to determine torque.

3.1.3. Data Acquisition System

In order to simplify data collection, DAQ hardware provided by NI is used. High speed data such as in-cylinder pressure and engine position are handled using an NI

9174 cDAQ; low speed data such as dynamometer load and emissions bench measurements are taken using a Fluke 287 multimeter. This is shown in Figure 6.

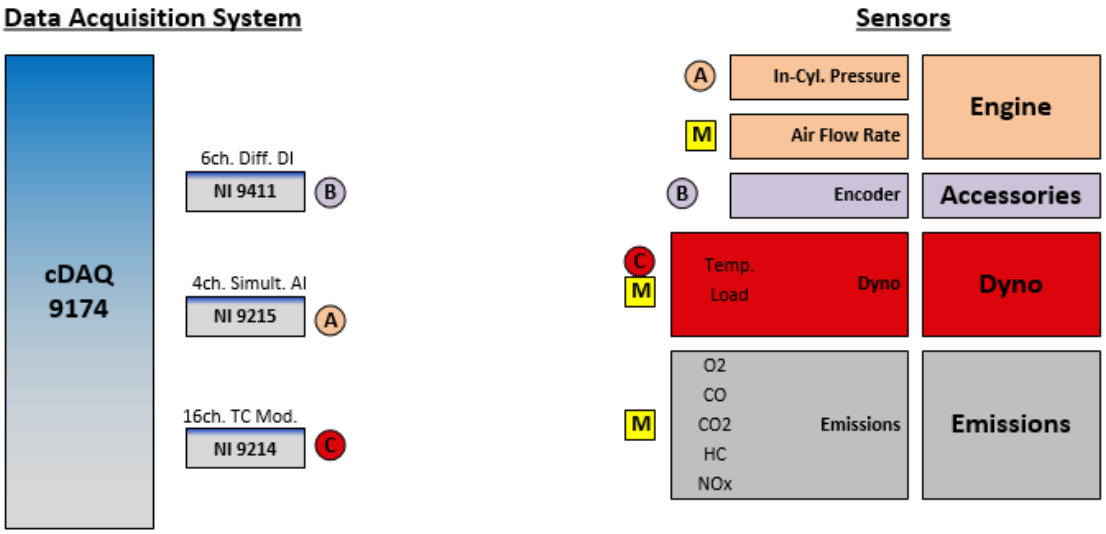

Figure 6. Each sensor shown paired with a corresponding module in the DAQ system or indicated by "M" to be measured with multimeter.

The sampling rate of each module is different. For example, the sampling rate of the NI 9752 module is 4,000 samples per second for each channel, whereas the NI 9205 module samples 250,000 times per second [27, 28]. This allows the DAQ system to capture enough data to prevent signal aliasing while not overloading the system with extraneous data.

3.1.4. Emissions Bench

Concentrations of CO, CO_2, THC, O_2, NO, and CH_4 in the exhaust stream are measured using a Horiba 200-Series emissions bench. A flame ionization detector is

used to measure HC's; a magneto-pneumatic technique to measure O_2, a chemiluminescent technique to measure NO, and non-dispersive infrared technique to measure CO and CO_2. A linearly calibrated output voltage is displayed on the analyzer and recorded.

Emissions are measured on a dry-basis. The sample line from the engine passes through a condenser to remove water vapor in the exhaust products. The dry sample is then pumped to a common rail from which each analyzer extracts a sample.

Each analyzer was tested for linearity using a Horiba SGD-710C gas divider, capable of blending ratios from 0% to 100% of upscale gas concentration in 10-percentage increments, with an accuracy of 0.5% of upscale gas concentration. The linearity results are shown in Appendix A.

3.1.5. Sensors

3.1.5.1. In-Cylinder Pressure

Pressure within the cylinder is measured using a piezoelectric pressure transducer. As pressure changes on the face of the piezoelectric crystal, the sensor outputs a charge proportional to this change in pressure. The charge signal is input into a charge amplifier, which transduces the charge signal into a voltage signal. The voltage signal is then fed into the DAQ, where a reading is taken at every 0.25 °CA.

The pressure transducer is mounted in the air-start port of the cylinder head. Without changing the cable, the transducer is periodically calibrated using a hydraulic calibration kit to reduce systematic uncertainty. Careful attention is paid to the tightening torque of 5.5 N-m applied to the mounting sleeve and 1.5 N-m applied to the transducer during calibration and reinstallation. During experimentation, 300 cycles are averaged to

reduce the impact of cyclic variation on the data from the state point [29]; however, 20 non-sequential individual cycles are recorded for each state point to specifically demonstrate cyclic variations. The charge amplifier is reset between each measurement to reduce signal drift.

3.1.5.2. Load Cell

Dynamometer load is transduced using an Omega LCCB-500 S-beam load cell. With an accuracy of 0.037% the full scale value of 500 lbs, the sensor is more than adequate to accurately measure the load of the dyno. As the sensor deflects under load, a strain gauge using a Wheatstone bridge changes in resistance. The change in resistance in the presence of a 10V excitation signal produces an output voltage proportional to the force applied to the sensor. Using calibration weights and the geometry of the dyno, the gain and bias of the voltage signal can be determined and used to calculate the force on the load cell. Using again the geometry of the dyno, the torque of the dyno can be calculated from the force on the load cell.

3.1.5.3. Encoder

Engine position is measured using a Dynapar HSD25 Series Optical Encoder. With 1440 ppr, the encoder can trigger measurements with the "A" signal every 0.25°CA. It also has a "Z" signal which is the index, or "trigger". This is used to set the crank-angle offset value to align crankshaft encoder with piston TDC.

The offset is found using a motoring curve. Once the engine is running, fuel is quickly cut off while the main power switch in the control box is turned off. This prevents the spark from firing, which prevents any combustion from occurring within the engine.

Due to the tremendous amount of kinetic energy stored in the flywheel, the engine continues to rotate for a considerable period of time, decelerating slowly. This provides the perfect opportunity to capture a motoring curve of in-cylinder pressure. The average of 10 cycles is captured immediately after fuel is cut off; another average of 10 cycles is captured when the engine has slowed by approximately 30%. Location of peak pressure is found in the two datasets and averaged. Assuming that peak pressure should occur roughly at TDC, the angular distance between the location of peak pressure and 0°ATDC is then set to be the encoder offset.

This value, however, does not properly locate TDC [29]. In reality, the peak pressure of a motoring curve occurs slightly before TDC. As the piston nears TDC, its velocity nears zero. As a result, the rate of energy input into the system by the piston slows while the rate of energy lost from the cylinder due to heat transfer remains high, due to the high temperatures of the compressed gas and high surface area to volume ratio. When the heat transfer rate is greater than the rate of energy addition provided by the piston, the cylinder pressure will decrease, even when TDC has not yet been reached. Blow-by losses past the piston rings also contribute to the decreasing pressure (i.e., loss of mass from the cylinder). The resulting angular distance by which the peak motoring pressure precedes TDC is called the thermodynamic loss angle.

Since the thermodynamic loss angle is related to piston speed and heat transfer behavior, it changes with engine speed. However, since a TDC indicator is unavailable, this value is assumed from literature to be -1.0°CA [29-31]. It is also assumed to remain constant over the operating envelope of the engine; this is reasonable to assume given the small range of studied engine speeds (i.e., 325 to 550 RPM).

3.1.5.4. Air Flow Meter

Volumetric flow of air into the engine is measured using a Meriam 50MC2 Series laminar flow element. Inside the element, there are hundreds of long, cylindrical capillaries in which the flow becomes laminar. The sensor then capitalizes on the Hagen-Poiseuille relationship between the laminar flow rate of a fluid in a long passageway of constant cross-sectional area and the pressure drop across the passageway [32].

Capable of a 400 SCFM flow rate, the laminar flow element outputs a pressure difference which is used in a quadratic relation to the volumetric flow rate with an accuracy of 0.8% of the reading. The pressure difference is read by a Dwyer Series DH Digihelic Differential Pressure Controller, which has an accuracy of 0.5% full scale. This transduces the differential pressure into a visual reading and a voltage.

3.2. Experimental Procedure

Before testing, the objective of the experiment is clearly defined. Necessary measurements are identified to accomplish the experimental objective. A test matrix is generated, targeting specific operating conditions of the engine.

Instruments are calibrated. Linearity of analyzers is checked, and analyzers are zeroed and spanned. Oil level in the engine is verified.

Shortly before the engine is started, safety protocols are obeyed. The engine is checked for debris or loose parts. Safety glasses are worn. A warning is given immediately preceding the engagement of the starter motor.

To begin testing, the engine is started. While idling, the dynamometer is connected by engaging the clutch lever. The dyno begins increasing load until reaching the value of the state-point being tested. The governor is adjusted to increase or decrease the speed of the engine to the value of the state-point being tested. The engine is then allowed sufficient time to reach a steady-state temperature, indicated by the coolant temperature. Once this has occurred, the coolant and exhaust temperatures are recorded.

The emissions bench is zeroed and spanned to ensure accuracy of measurements. Once the calibration of every analyzer is confirmed, they are purged with nitrogen for one minute to clear them for testing. The bench is then set to sample mode, and after one minute, the reading from each analyzer is recorded 10 times.

After recording the emissions data, in-cylinder pressure is recorded. Data for an average of 300 cycles are recorded as well as 10 non-sequential individual cycles. It should be noted that the individually-recorded cycles are not consecutive. The charge amplifier is reset between each measurement to minimize signal drift. During the time when 300 cycles are being recorded, 10 readings of the differential pressure transmitter are captured; this is the pressure differential across the laminar flow element used to calculate air volumetric flow rate. Also, the voltage from the load cell on the dynamometer is measured five times with a multimeter and recorded. Once all the measurements have been performed and recorded, the load is then adjusted to the value of the next state point, and the process repeats.

3.3. Test Matrix

The test matrix used for the experiment consists of a speed and load sweep. This is used to show the independent impact of speed or load on the in-cylinder pressure and emissions. The test matrix is shown in Table 3.

Table 3. Test matrix of experiment listing the operating point label for each condition.

Load (% Full Load)	Speed (RPM) 350	375	400	425	450	475	500	525
50	01	02	03	04	05	06	07	08
63	09	10	11	12	13	14	15	16
74	17	18	19	20	21	22	23	24
84	25	26	27	28	29	30	31	32
93	33	34	35	36	37	38	39	40
100	41	42	43	44	45	46	47	48

Notice that operating points 41-43 are darkened. During the experiment, it was found that the engine could not statically maintain these operating conditions. Once set, the engine speed would drift slightly, causing the load to change, which accelerated the drift in speed. Thus, these three operating points were removed from the experiment. This eliminated the possibility of making comparisons with operating conditions at 100% load and 350 to 400 RPM.

The full load condition has been experimentally determined as a function of speed. The condition of 100% load is defined as the torque output of the engine at which the engine would begin to stall (i.e., the dyno was applying too much load at the

given speed set point). By applying exactly half of this torque value, for example, the condition of 50% load is attained.

3.4. Calculations

The measurements provided by the emissions bench analyzers are in units of Volts and are specific to the range in which the measurements were performed. The concentration of each species, C, in ppm is calculated using the equation,

$$C = A_V \frac{R}{D} \tag{1}$$

where A_V is the analyzer voltage, R is the concentration of the range in parts per million (ppm), and D is the reading at full scale. Thus, for example, if an analyzer voltage, A_V, of 0.700V is read while the measurement is taken in a range, R, of 8000 ppm, and the reading at full scale, D, is 1.000V, then the measured concentration, C, is 5600 ppm.

Random error, S, is due to statistical uncertainties and is quantified using Equation (2) below, where $t_{0.025,\upsilon}$ is Student's "T" table value corresponding to a confidence level of 95% and υ degrees of freedom [33], σ is the standard deviation of the samples, and N is the number of samples. Systematic error, B, is error introduced by the measurement device. Total uncertainty of a measurement is found using Equation (3) below.

$$S = t_{0.025,\upsilon} \frac{\sigma}{\sqrt{N-1}} \tag{2}$$

$$U_{X_1} = \sqrt{S^2 + B^2} \tag{3}$$

When using multiple measurements to calculate a value, error propagates through each of the measurements into the result. To quantify the error in the calculated value,

the Kline-McClintock [34] propagation equation is used, shown in Equation (4) below. In this equation, the partial derivatives of the function F are taken with respect to each of the N variables that contribute error. The partial derivative is then multiplied by the uncertainty of the variable at which it was evaluated; the square root of the sum of the squares of these products is then taken.

$$U_T = \sqrt{\left(\frac{\partial F}{\partial X_1} U_{X_1}\right)^2 + \left(\frac{\partial F}{\partial X_2} U_{X_2}\right)^2 + \cdots \left(\frac{\partial F}{\partial X_N} U_{X_N}\right)^2} \tag{4}$$

The density of air is calculated using the ideal gas relation presented in Equation (5) below, where P is the absolute pressure, R is the gas constant for air, and T is the absolute temperature.

$$\rho = \frac{P}{RT} \tag{5}$$

The volumetric flow rate of air is calculated using the equation of the factory-provided calibration curve [35], shown in Equation (6) below, where α and β are calibration constants provided by the manufacturer, and dP is the change in pressure across the laminar flow element.

$$\dot{\forall}_{air} = \alpha(dP) + \beta(dP)^2 \tag{6}$$

The factory-provided calibration curve is certified until the date of September 7, 2015. This means that the measurements from this device are trustworthy. Volumetric flow rate values were predicted as a function of speed by multiplying the total cylinder volume (10.57 L) by the engine speed. These served as a rudimentary comparison to further demonstrate credibility of air flow measurements.

Mass flow rate of air is calculated using the density and volumetric flow rate in Equation (7).

$$\dot{m}_{air} = \rho \dot{\forall}_{air} \tag{7}$$

Torque applied by the dynamometer is calculated using Equation (8), where G is the calibration gain, and $Bias$ is the calibration bias. The linearity results for the load cell are presented in Appendix A. The power output of the engine is calculated using Equation (9), where ω is the engine speed in RPM, and τ is torque in ft-lbs.

$$\tau = GV + Bias \tag{8}$$

$$hP = \frac{\tau\omega}{5252} \tag{9}$$

The air-fuel ratio of the total engine system is found using Heywood's equation [23] below. Terms in brackets represent concentration measurements of that species, and K_f is given by Equation (11) below. This equation is a function of the hydrogen-carbon ratio of the fuel, y, which is determined by the information in Table 2.

$$AFR_{act} = K_f \frac{\left(\frac{1}{4}[CO] + [CO_2] + [O_2] + \frac{y}{4}([CO] + [CO_2]) + \frac{[NO]}{2}\right)}{[CO] + [CO_2] + [THC]} \tag{10}$$

$$K_f = \frac{138.18}{12.011 + 1.008y} \tag{11}$$

The stoichiometric air-fuel ratio is determined by Equation (12), shown below. In this equation, M_{air} is the molecular weight of air, and M_{fuel} is the molecular weight of the fuel.

$$AFR_{stoich} = \frac{M_{air}}{M_{fuel}}\left(\frac{1+\frac{y}{4}}{0.21}\right) \tag{12}$$

Using the values calculated in Equations (10) and (12), the equivalence ratio, ϕ, is found using Equation (13).

$$\phi = \frac{AFR_{stoich}}{AFR_{act}} \tag{13}$$

From this value and the mass flow rate of air, the BSFC is calculated using Equation (14).

$$BSFC = \frac{\dot{m}_{air}}{AFR_{act}P} \tag{14}$$

Emissions of NO normalized to engine power output, or brake specific NO emissions, are calculated using Equation (15).

$$bsNO = \frac{C_{NO}}{10^6}\left(\frac{M_{NO}}{M_{exh}}\right)(1 + AFR_{act})(BSFC) \tag{15}$$

where C_{NO} is the concentration of NO in ppm, M_{NO} is the molecular weight of NO, and M_{exh} is the molecular weight of exhaust products (approximated by the molecular weight of air).

The delivery ratio is also calculated at each operating condition using Equation (16). Delivery ratio is defined, in a homogeneous charge engine, to be the ratio of the mass of the fuel-air mixture delivered to the cylinder to a reference mass. In this equation, $\forall_d$ is the displacement volume, and ρ_{ch} is the density of the fresh charge.

$$\Lambda = \frac{\dot{m}_{air}\left(1 + \frac{1}{AFR_{act}}\right)}{\forall_d \rho_{ch} \omega} \tag{16}$$

Trapping efficiencies can be specifically determined for air and fuel using exhaust concentrations [23]. The trapping efficiency of air is the ratio of air trapped in the cylinder to air supplied through the intake port. It is also equal to unity minus the ratio of short-circuiting air to air supplied through the intake port [36]. The amount of short-circuiting air is determined by using the fuel mass flow rate, air-fuel ratio, measured concentration of O_2 in exhaust, and an approximate molecular weight of exhaust products. The amount of supplied air is determined by using the fuel mass flow rate, air-fuel ratio, approximate mass fraction of oxygen in air, and approximate molecular weight of exhaust products. These terms combined form Equation (17).

$$\eta_{tr,air} = 1 - \frac{(1 + AFR_{act})[O_2]_{exh}}{AFR_{act}[O_2]_{atm}} \tag{17}$$

The equation used to determine the trapping efficiency of fuel is given by Equation (18). This equation calculates the ratio of the mass of carbon in the cylinder after combustion and before exhaust port open (EPO) to the mass of carbon delivered to the cylinder. The mass of carbon trapped in the cylinder is assumed to be completely converted to CO and CO_2. The mass of carbon delivered to the cylinder either gets trapped in the cylinder and converted to CO or CO_2, or it short-circuits into the exhaust stream as THC emissions.

$$\eta_{tr,fuel} = \frac{[CO] + [CO_2]}{[CO] + [CO_2] + [THC]} \tag{18}$$

Since each of the emissions measurements are concentrations with respect to exhaust products, it can be shown that the ratio of these concentrations is also representative of ratio of masses. Also, it is worth noting that in a homogeneous charge, spark-ignited engine, the value of the trapping efficiency of air should be roughly equivalent to that of fuel.

The scavenging efficiency is the ratio of the mass of fresh charge of fuel-air mixture retained to the mass of the cylinder at exhaust port close (EPC). This is different from the delivery ratio in two ways. First, the scavenging efficiency describes the amount of fresh charge retained in the cylinder. The delivery ratio describes the amount of fresh charge that is sent to the cylinder, whether it is retained or short-circuits. Second, the reference mass used in the delivery ratio is evaluated at ambient conditions while the reference mass used in the scavenging efficiency is evaluated at conditions at EPC. The scavenging efficiency is calculated using Equation (19),

$$\eta_{sc} = \Lambda \eta_{tr} \frac{P_0 \forall_D T_b}{P_b \forall_b T_0} \tag{19}$$

where P_0 is the ambient pressure, P_b is the pressure at EPC, $\forall_b$ is the cylinder volume at EPC, T_b is the cylinder temperature at EPC, and T_0 is the ambient temperature. The pressure at EPC was assumed to be the average of all data points – 350 kPa_{abs}; the temperature at EPC was assumed to be 450 K (350°F) [37].

The cyclic COV of IMEP is calculated for each operating point. This is used as a measure of the cyclic variation at each operating point. Equation (20) details this calculation,

$$COV_{IMEP} = \frac{\sigma_{IMEP}}{IMEP} \tag{20}$$

where σ_{IMEP} is the standard deviation of the $IMEP$ over a sample of 300 consecutive cycles, which is calculated using Equation (21) below.

$$IMEP = \frac{\sum_{i=1}^{N} P_i \Delta \forall_i}{\forall_d} \tag{21}$$

In this equation, N is the number of encoder bits, P_i is the pressure at the i^{th} encoder bit, and $\Delta \forall_i$ is the change in cylinder volume at the i^{th} encoder bit. To obtain $\Delta \forall_i$ at all crank angle bits, the cylinder volume as a function of crank angle is obtained using the equation,

$$\forall = \forall_C + \left(\frac{\pi B^2}{4}\right)\left((a + l) - \left(a\cos\theta + \sqrt{l^2 - (a\sin\theta)^2}\right)\right) \tag{22}$$

where $\forall_C$ is the clearance volume, B is the bore diameter, a is the crank radius, l is the connecting rod length, and θ is the angular position of the crankshaft [38]. The value of $\Delta \forall_i$ is then calculated using a first-order central difference method [39] given in Equation (23).

$$\begin{aligned} for\ i = 1 \qquad & \Delta \forall_i = \forall_i - \forall_{i+1} \\ for\ i = 2{:}\,N - 1 \qquad & \Delta \forall_i = \frac{\forall_{i-1} - \forall_{i+1}}{2} \\ for\ i = N \qquad & \Delta \forall_i = \forall_{i-1} - \forall_i \end{aligned} \tag{23}$$

4. RESULTS AND DISCUSSION

Using the aforementioned equipment, test matrix, procedure, and calculations, results are presented. These results are discussed within the framework provided by Chapters 1 and 2 of this document, which detail how speed and load impact cyclic variation as well as many other engine parameters. Trends predicted in Chapter 2 are compared with these results, beginning with torque measurement at each operating condition.

4.1. Engine Load

As mentioned previously, 100% load is defined as the torque output of the engine at which the engine would begin to stall (i.e., the dyno is applying too much load at the given speed set point). This torque was determined for each speed used in the test matrix. The measured torque at each operating condition is presented in Figure 7.

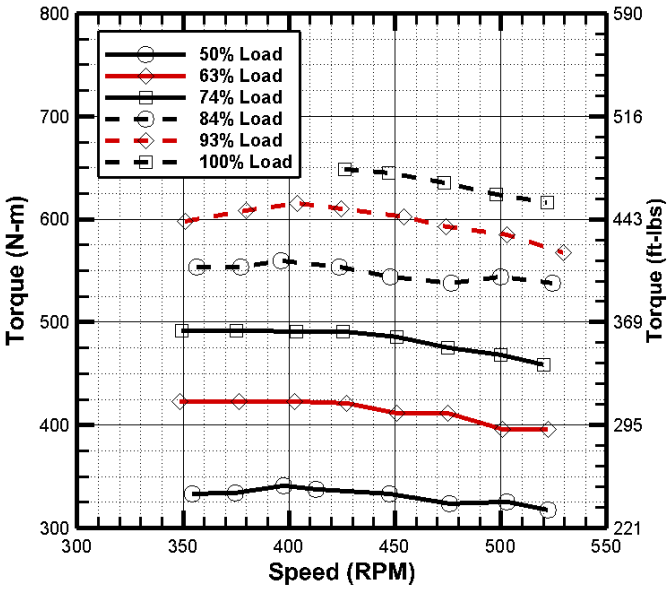

Figure 7. Measured torque as a function of speed and percent load.

The rated maximum continuous torque of the engine is 540 N-m specified by the manufacturer. Manuals from the manufacturer, however, show the engine is capable of significantly higher load than the specified rating, which is why 540 N-m is not the definition of 100% load in this experiment. The measured torque at 100% load was as high as 650 N-m, occurring at 425 RPM. The condition of 50% load at 425 RPM, for example, is then defined to be 325 N-m; the measured torque at this operating condition is approximately exactly that value – 335 N-m. Figure 7, then, is the measured matrix of loads and speeds at which all other measurements are taken.

4.2. Cyclic Variation

The COV of IMEP provides a measure of the cyclic variation of an operating point [42]. This value was calculated for each operating point, and the data are shown in Figure 8.

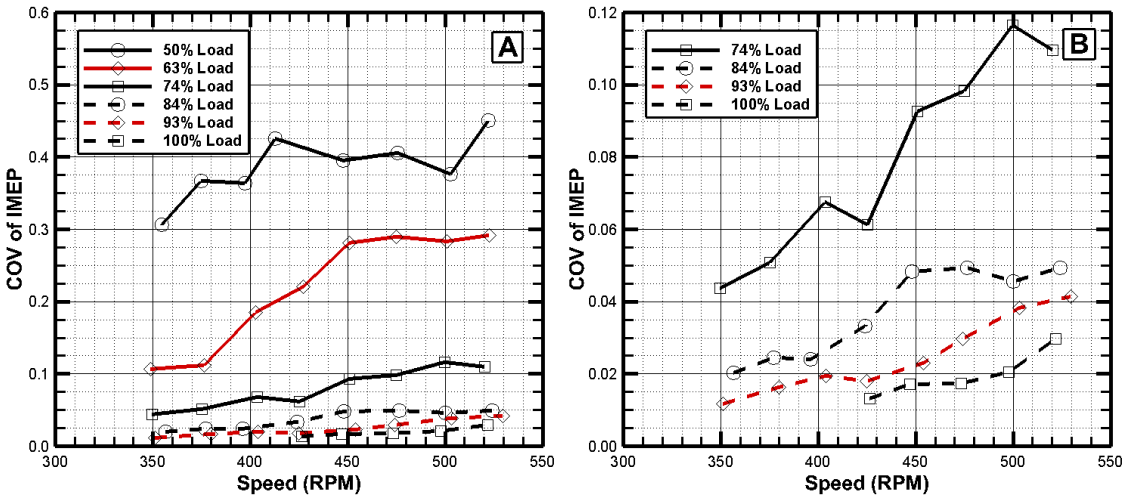

Figure 8. Cyclic-COV of IMEP over 300 cycles as a function of speed and load (A) for all loads and (B) for loads at and above 74%.

The effect of engine load is evident in the COV of IMEP results. Increasing engine load dramatically increases engine stability. For example, at 350 RPM and 50% load, the COV of IMEP is 31%; at 93% load, it's 1.2%. At high speeds, the trend is the same. At 525 RPM and 50% load, the COV of IMEP is 45%; at 93% load, it's 4.1%. Increasing load from 50% to 93% provides an order of magnitude in increased engine stability at all tested engine speeds. This agrees with the predicted trend presented in Chapter 2, and could be a result of better scavenging, specifically near the spark plug.

The results show speed also having a significant effect on the stability of the engine, particularly at low load conditions. At low speed, the engine is most stable at a given load. For example, at 50% load and 350 RPM, the COV of IMEP is 31%; at the same load and at an increased speed of 425 RPM, the COV of IMEP is 43%; at a speed of 525 RPM, the COV of IMEP is 45%. Similarly, at 93% load and 350 RPM, the COV of IMEP is 1.2%; at 425 RPM, it's 1.8%; at 525 RPM, it's 4.1%. The finding of increasing cyclic variation with increasing speed agrees with the predictions presented in Chapter 2, and are likely a result of stronger turbulence inhibiting flame kernel growth.

The lack of error on these results is worthy of mention. The COV of IMEP is simply the standard deviation of the measured IMEP values divided by the average IMEP. Statistical uncertainty arises when the population average cannot be determined. Since the entire population of the 300 values of IMEP in this case is quantified, however, there is no statistical uncertainty on the COV of IMEP calculations.

4.3. Air and Fuel

Air volumetric flow rate was measured at each operating condition, and the data are shown in Figure 9. The uncertainty on these measurements is very high. Since the engine is a single cylinder, it is constantly cycling between high air-flow and air-stoppage conditions. As the piston travels towards TDC, the reed valves in the intake manifold open. Air is drawn into the stuffing box by the low pressure created by the travelling piston (moving toward TDC). As the piston reverses direction and travels towards BDC, however, the reed valves in the intake manifold close, stopping flow in the intake pipe. The laminar flow element experiences this cycle between approximately five to eight times per second, depending on the speed of the engine. Because of this, the reading of the pressure drop across the laminar flow element is extremely erratic, creating a large statistical uncertainty within each data point.

Nevertheless, it can be seen that there is an identifiable trend with speed. There is a statistically significant difference at a 90% confidence level between the air flow rate at 475 RPM and 350 RPM, and again between 525 RPM and 475 RPM. The data show an increase in the air flow rate as a function of speed, which is likely due to the greater number of intake events in the engine. Values of volumetric flow rate of air demonstrate agreement with predicted values. Though these comments can be made for speed, no statistically meaningful observations can be made regarding the impact of load on air flow rate.

The equivalence ratio, results for which are shown in Figure 10, is calculated using Equations (10)-(13) based primarily on emissions results. Results show a clear

trend with load; as load increases, equivalence ratio increases towards stoichiometric. The equivalence ratio also tends to decrease with increasing speed. Values show that the engine burns slightly lean at low speeds and high load and burns significantly lean at high speeds and low load.

BSFC is calculated and shown in Figure 11. Trends as functions of speed or load are impossible to state with 95% confidence. This is due to the use of the highly-uncertain air flow rate measurement, shown in Equation (14).

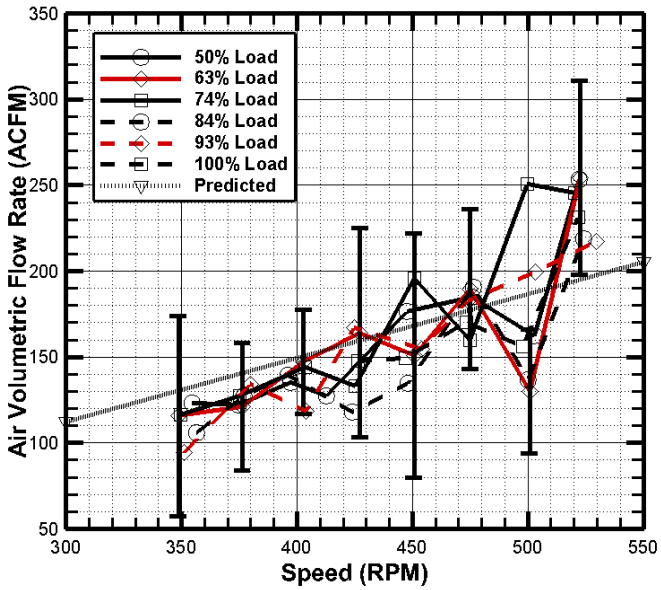

Figure 9. Air volumetric flow rate as a function of speed and load is shown with error bars on the 63% load dataset corresponding to 90% confidence.

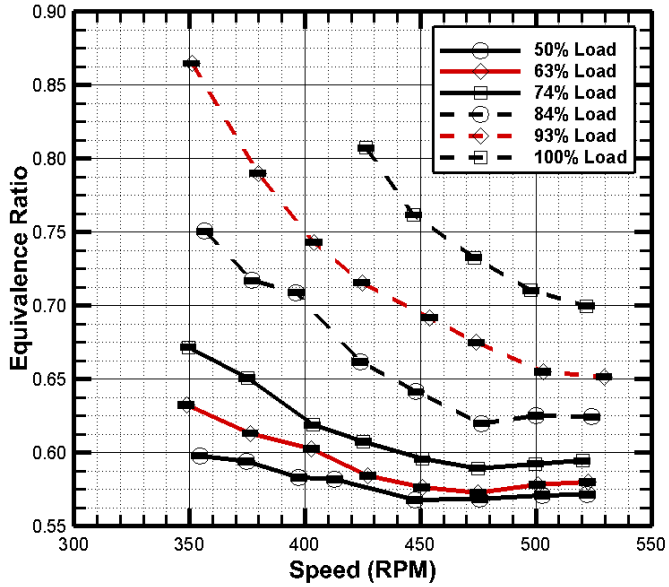

Figure 10. Calculated results for equivalence ratio as a function of speed and load.

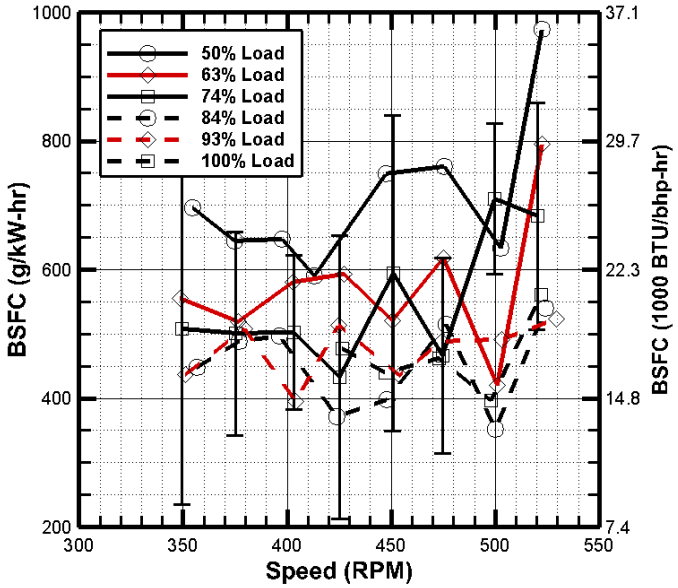

Figure 11. BSFC as a function of speed and load with error bars on the 74% load dataset corresponding to 95% confidence.

The delivery ratio of the engine, shown in Figure 12, has considerable uncertainty, again due to its dependence on measured air flow rate. A trend as a function

of speed or load is impossible to determine with reasonable certainty. Nonetheless, observations can still be made. First, the average delivery ratio is over 1.0 at most operating conditions. This either suggests that the charge density is somehow greater than expected, or it suggests a loss of mass in the cylinder due to short-circuiting behavior. The latter is more likely, particularly at low engine speed. Second, it can be stated with 95% confidence that the delivery ratio at 350 RPM is between 0.45 and 1.55; the delivery ratio at 525 RPM is between 0.85 and 1.85. Since trends cannot be made with respect to speed or load, however, correlation with cyclic variation is difficult.

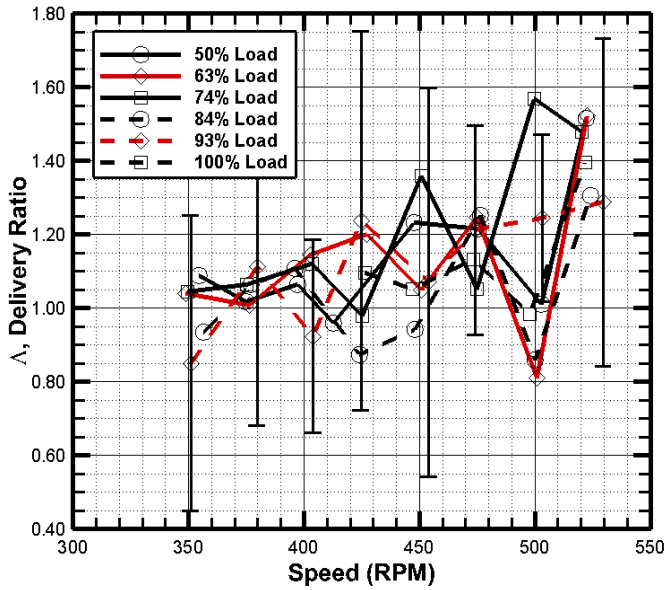

Figure 12. Delivery ratio as a function of speed and load with error bars on the 93% load dataset corresponding to 95% confidence.

The trapping efficiency of fuel is shown in Figure 13A. Results are between 35% and 43%. Demonstrating a complex interaction with speed and load, a consistent

trend between any of these parameters is difficult to determine. Fuel trapping efficiency seems to increase from 350 RPM to 375 RPM at all loads. From 375 to 500 RPM, however, it tends to decrease. Then from 500 to 525 RPM, the data suggests an increasing trend again. These results seem to follow the trend captured in the findings of Blair and Kenny [44]. Trapping efficiency increases, decreases, then increases again. Also, the generally decreasing trend of trapping efficiency with increasing speed in Figure 13A correlates well with the generally increasing trend of delivery ratio with increasing speed, shown in Figure 12. Blair and Kenny also confirm this inverse relationship in their study.

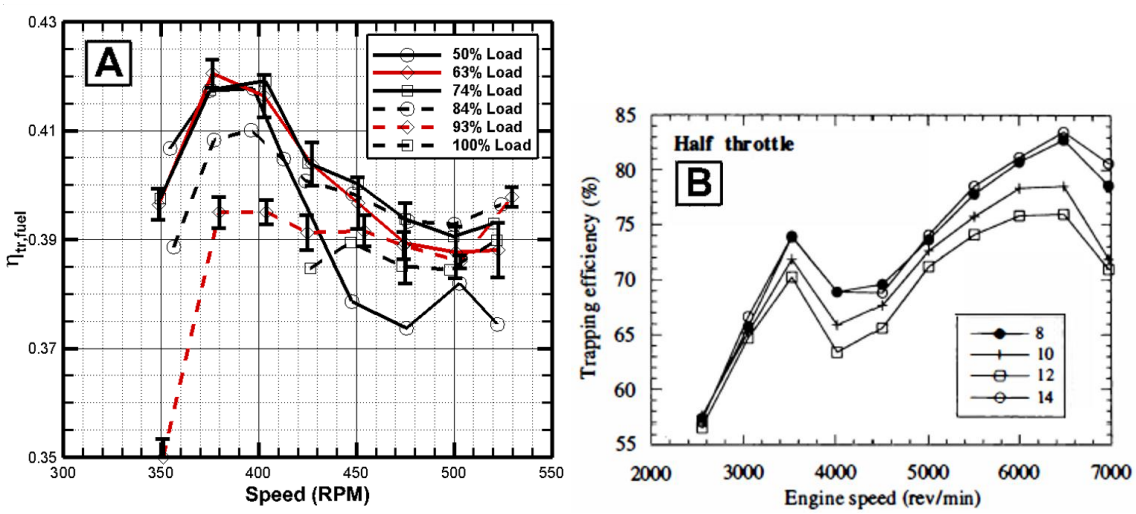

Figure 13. (A) Calculated values of trapping efficiency of fuel as functions of speed and load with error bars shown on the 63% and 93% load datasets corresponding to 95% confidence and (B) data from Blair and Kenny showing trapping efficiency as a function of speed and port geometry [44].

The trapping efficiency of air is shown in Figure 14. These results show remarkable resemblance to those of the equivalence ratio, shown in Figure 10. The values of air trapping efficiency are consistently between 19% and 32%, which are extremely low. Air trapping efficiency demonstrates a decreasing trend with increasing speed and an increasing trend with increasing load. Thus the highest values are at low speed and high load.

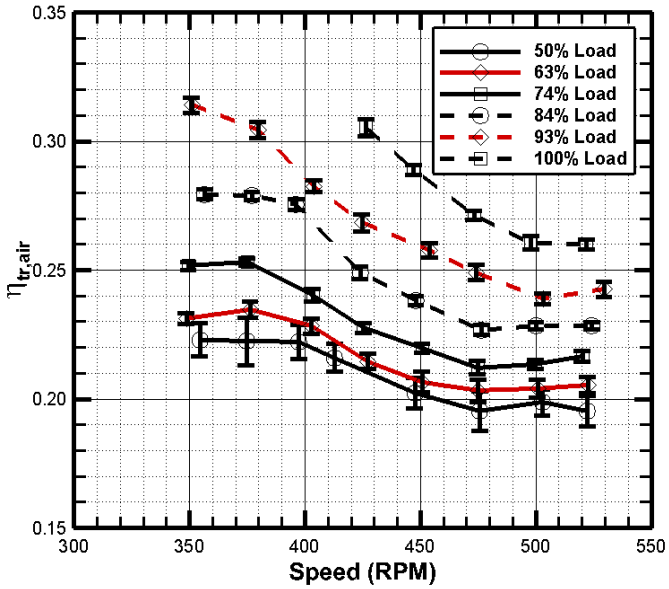

Figure 14. Calculated values of trapping efficiency of air as functions of speed and load with error bars shown on the datasets corresponding to 95% confidence intervals.

Comparisons between fuel and air trapping efficiencies reveal a problem with the data. Fuel and air trapping efficiencies should agree with each other, since this is a cross-scavenged homogenous charge engine [23]. The values for air trapping efficiency are suspected to be incorrect. The equation used to calculate these values, Equation (17),

is to be used for stoichiometric or rich-burning engines. The engine used in this study has been shown to generally burn lean. Exhaust O_2 emissions are a combination of short-circuited air and exhaust products. The equation requires measurement of the concentration of O_2 in the cylinder after combustion and before EPO. This is the in-cylinder concentration post-combustion, which is different from the concentration in the exhaust stream due to short-circuiting air.

Naturally, if the trapping efficiency is not correct, the scavenging efficiency cannot be correct, since it uses the trapping efficiency in its calculation. The scavenging efficiency is shown in Appendix C for reference. Average results are between 95% and 195%; results greater than 100% are impossible. These discrepancies serve as future work as the only way to improve these characterizations is to directly measure fuel flow, which is presently not possible with the architecture of the fuel system (pressure drop across flow meter is too high for the proper operation of the engine).

4.4. Emissions

Emissions data for CO, CO_2, THC, O_2, and NO were taken at each operating point. CO emissions data, shown in Figure 15, have considerable uncertainty due particularly to systematic uncertainty. Because the emissions are being evaluated in a 5000 ppm range, the resolution of the detector contributes significant uncertainty to the measurement. Nonetheless, the data still are able to show trends due to load.

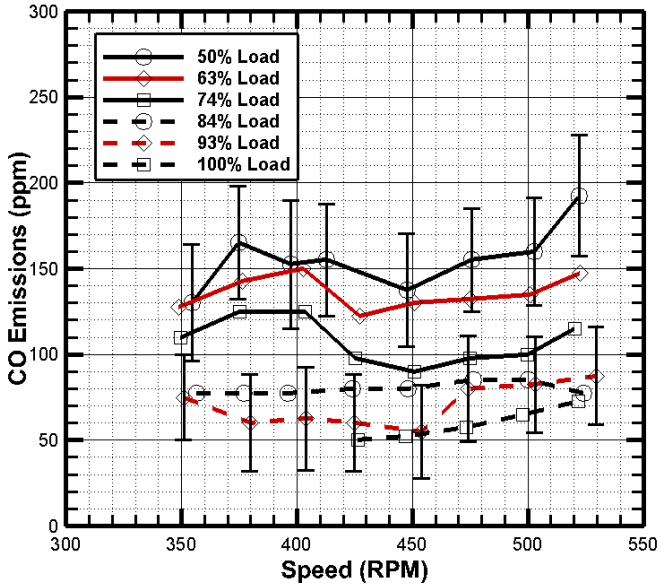

Figure 15. CO emissions as a function of speed and load with error bars, corresponding to 95% confidence, shown on the 50% load and 93% load datasets.

The uncertainty of the measurements makes it difficult to draw conclusions about the effect of speed on CO emissions. Since the error bars of the CO measurement at 350 RPM overlap with those at 525 RPM at each load, the effect of speed on the emissions level cannot be stated with 95% confidence. However, it can be said, with 95% confidence, that increasing the load from a low load, such as 50%, to a high load, such as 93%, decreases the CO emissions. This is likely due to the decrease in partial burning combustion events with increasing load. As heat is released earlier in the expansion stroke due to the increased load, the reactants have more opportunity to reach complete products of combustion. This means a decrease in CO production and an increase in combustion efficiency and CO_2 emissions levels [45]. Thus, cyclic variation, as it

decreases with increasing load, correlates with a decrease in CO emissions. This agrees with the expectations in the literature presented in Chapter 2.

The CO emissions trend well with those of CO_2, shown in Figure 16. With increasing load, CO_2 emissions increase, which compliments the decreasing trend of CO. It is also clear that CO_2 production decreases with increasing speed over most of the operating envelope of the engine, except at 350 RPM. This matches the trend of combustion stability, which decreases with speed. However, where the effect of speed is diluted with increasing load, the effect of speed on CO_2 shows, in any obvious way, no such trend. For example, at a load of 93% and a speed of 400 RPM, the volume fraction of CO_2 is 3.2% while at 525 RPM it's 2.8%; at a load of 63%, the volume fraction of CO_2 is 2.7% at 400 RPM and 2.4% at 525 RPM. The different loading conditions did not significantly affect the difference between the emission levels of the two speeds.

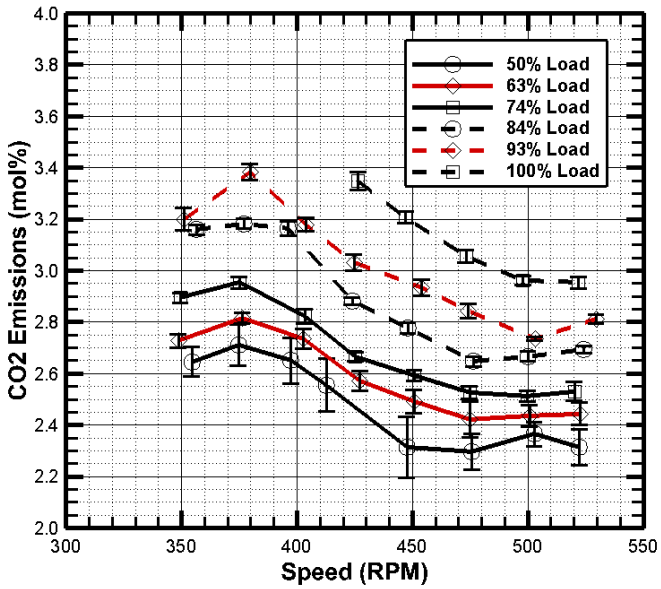

Figure 16. CO_2 emissions as a function of speed and load.

Thus, as cyclic variation decreases with increasing load, CO_2 increases, indicating greater combustion efficiency. Also, since the CO_2 emissions trend decreasingly with speed, CO emissions could be suspected to increase with increasing speed. This would correlate well with cyclic variation; as it increases with increasing speed, more frequent events of partial burn could elevate CO levels. Though this would disagree with an expectation from literature, the experiment used to set forth this expectation used engine speeds an order of magnitude higher than those in the present study. This disagreement, therefore, is acceptable. Regardless, this hypothesis can be tested in future research with higher accuracy in the CO measurement.

THC emissions are also recorded, shown in Figure 17. At low speed and low load, a distinct behavior is unapparent. This is likely due to the extremely erratic behavior of the engine at high speed and low load; it is not surprising that a consistent emissions behavior cannot be determined at such an inconsistent operating condition.

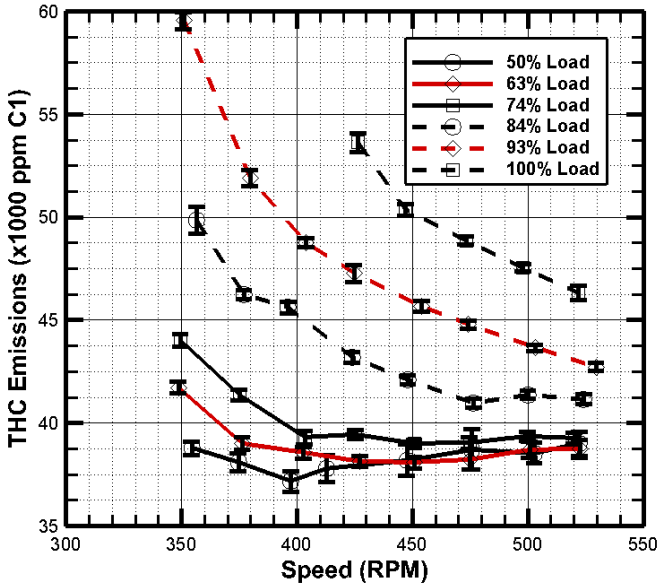

Figure 17. THC emissions as a function of speed and load.

At low load and low speed, a pattern is more obvious. At all tested loads, increasing the speed from 350 RPM to 400 RPM causes THC emissions decrease. At the highest load, the same change in speed produces the greatest decrease in THC emissions. For example, at 93% load, THC emissions are 59,500 ppm (C_1) at 350 RPM and decrease to 48,700 ppm (C_1) at 400 RPM; at 50% load, THC emissions are 38,700 ppm (C_1) at 350 RPM and decrease to 37,000 ppm (C_1) at 400 RPM. The same decrease in speed caused a decrease of 10,800 ppm (C_1) at 93% load, while only resulting in a decrease of 1,700 ppm (C_1) at 50% load.

THC emissions increase with increasing load. This defies an expected trend. It is expected that since cyclic variation decreases with increasing load, there are fewer cycles of misfires or partial-burn, which would result in lower THC emissions in the exhaust stream. Results, however, show the opposite trend. This may be due to an

increase in fuel flow rate. As load is increased, the throttle is opened allowing more fuel into the cylinder; this can be seen in the results of equivalence ratio. Thus, even with more stable combustion at higher loads, the increase in fuel could be dominating the decrease in emissions due to decreasing misfires and partial-burn. This could explain the increase in THC emissions as load increases.

The increasing trend with increasing load is magnified at low speeds. For example, at 525 RPM and 74% load, the THC emissions concentration is 39,200 ppm (C_1), and at 93% load, it's 42,800 ppm (C_1); at 350 RPM and 74% load, the THC emissions concentration is 43,500 ppm (C_1), and at 93% load, it's 58,800 ppm (C_1). It seems that a decrease in speed intensifies the effect of load.

Concentration of O_2 in the exhaust products, shown in Figure 18, trend with equivalence ratio, particularly in lean-burning conditions [46, 47]. From the data of this study, O_2 concentration decreases with increasing load. This is likely due to the apparent decrease in cyclic variation shown in Figure 8. A decrease in O_2 exhaust concentration indicates an increase in equivalence ratio [38], which agrees with the equivalence ratio results shown in Figure 10. Concentration of O_2 also shows dependence on speed, generally increasing with increasing speed, which trends with the decreasing equivalence ratio. This is likely due to the increased cyclic variation at higher speeds, where partially-burning cycles would leave O_2 unburned or misfiring cycles would leave all of the O_2 unburned.

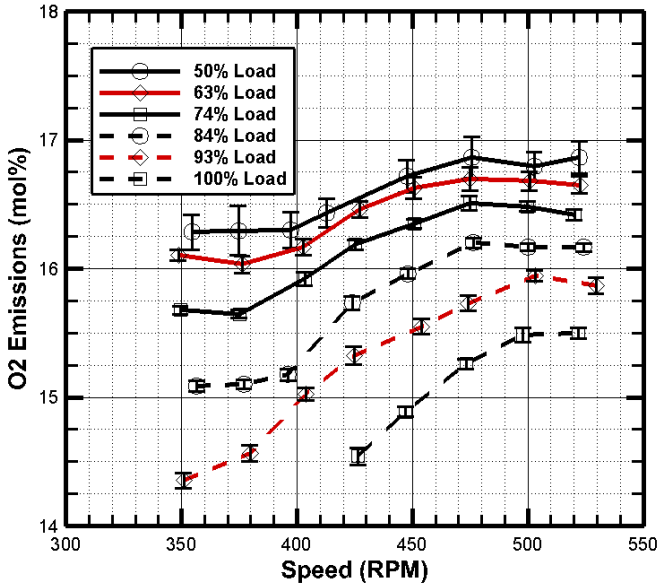

Figure 18. O_2 concentration in exhaust products as a function of speed and load.

Concentrations of NO, shown in Figure 19, demonstrate a trend with load. At speeds greater than or equal to 450 RPM and loads at or below 74%, the trend is unclear. However, at higher load, increasing engine load strongly increases NO production. This occurs only with the exception of the operating point at 93% load and 350 RPM. High NO production at these operating conditions also correlate with equivalence ratio results presented in Figure 10. At high load, the overall system is shown to be close to stoichiometric, which leads to the highest adiabatic flame temperature. This would drive the thermal mechanism of NO production, leading to high emission levels. At low load, NO production is exponentially lower. This could be a result of poor scavenging, which would result in a higher residual fraction and serve as a crude form of exhaust gas recirculation (EGR); this correlates with increasing cyclic variation as load decreases.

Concentrations of NO also show dependence on speed. At the lowest load, a trend as a function of speed cannot be stated with 95% confidence due to systematic uncertainty. However, at loads at and above 84%, a clear trend emerges where NO production decreases with increasing speed. Again, this correlates with increasing cyclic variation, which could be increasing the exhaust residuals because of worsening scavenging. The only exception to this trend is at 93% load as speed increases from 350 RPM to 375 RPM. Future research could be conducted to investigate and validate this anomaly.

BSFC is shown as a function of brake-specific nitric oxide emissions (bsNO) are shown in Figure 20. There is exponential increase in bsNO at higher load. Again, this is likely related to the improved scavenging, apparent by the reduction in cyclic variation, which reduces the amount of diluting exhaust residuals in the cylinder. Also, the data seems to generally follow a 90° bending trend-line, where BSFC decreases with no significant change to bsNO or bsNO changes with no significant change to BSFC.

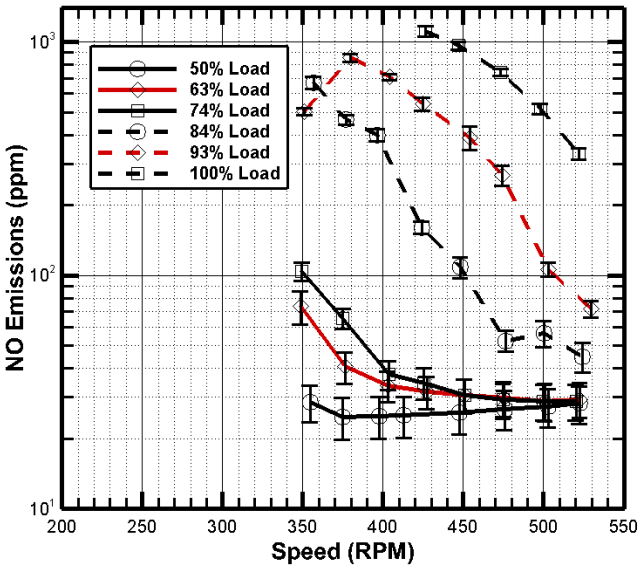

Figure 19. NO emissions as a function of speed and load.

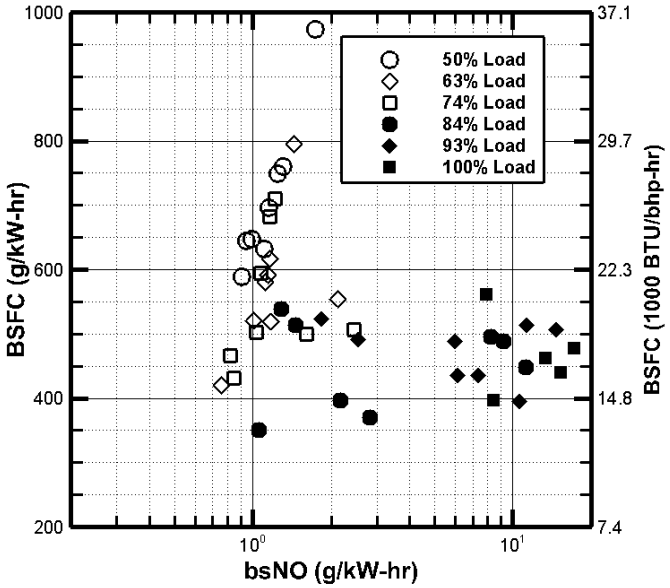

Figure 20. BSFC as a function of bsNO for each operating condition.

CH_4 emissions, shown in Figure 21, are difficult to interpret. The statistical uncertainty on the measurements that were made within the range of the analyzer is high,

making a speed trend impossible to determine with confidence. This could be due to the extreme cyclic variation experienced at these operating conditions. Misfires result in the emissions of all of the fuel contained in a fresh charge, which sporadically spike the HC emissions measurements. Also, the analyzer only measured up to 20,000 ppm CH_4 (C_1). At and above loads of 74%, the readings were above the analyzer limit.

The results do show, however, that CH_4 emissions increase with increasing load. This is evident from higher loads being consistently above the analyzer limit. Also, these results show that the CH_4 emissions are above 19,000 ppm (C_1) at all speeds and loads. This means that CH_4 emissions cannot comprise less than 46% of the HC emissions at loads at or lower than 63%, and they cannot comprise less than 33% of HC emissions at loads at or higher than 74%.

To summarize the reactions of CO, CO_2, O_2, NO, THC, and CH_4 results are detailed in Table 4. The correlation between each parameter and both speed and load is listed. However, instead of making the connection from each parameter to speed or load, a connection is evident from each parameter to cyclic variation. For example, NO has an inverse correlation to COV of IMEP – when COV of IMEP increases, NO tends to decrease, and vice versa. Thus, O_2 is shown (and CO is suspected) to correlate directly with COV of IMEP, while CO_2, NO, and THC are shown (and CH_4 is suspected) to correlate inversely with COV of IMEP.

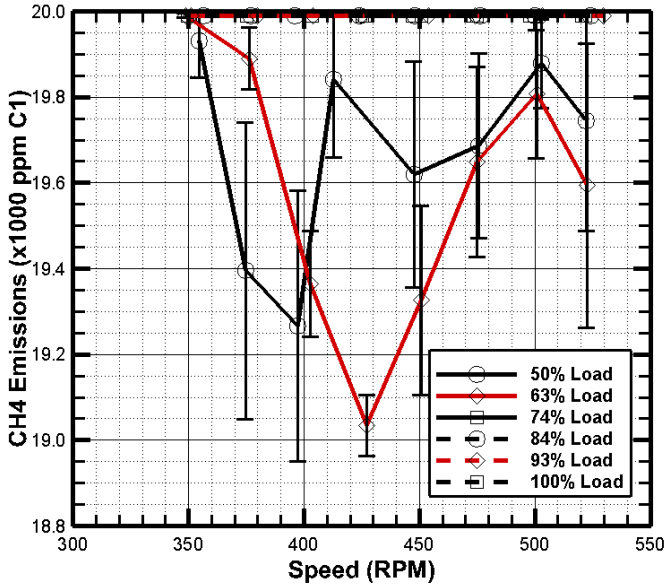

Figure 21. CH_4 emissions as a function of speed and load.[1]

Table 4. Correlation trends between speed, load, COV of IMEP, and emissions.

Parameter	Increasing Speed	Increasing Load
COV of IMEP	Direct	Inverse
CO	Direct [2]	Inverse
CO_2	Inverse	Direct
O_2	Direct	Inverse
NO	Inverse	Direct
THC	Inverse	Direct
CH_4	Inverse	Direct

[1] Data points above 20,000 ppm (C1) of methane are beyond analyzer range.
[2] This trend is hypothesized, not experimentally determined.

4.5. In-Cylinder Pressure

Cylinder pressure measurements can qualitatively display some of the trends previously mentioned, particularly cyclic variation. Each operating condition demonstrates unique behavior which can be quantified by COV of IMEP data presented in Figure 8 and correlated with the trends of other measurements. The pressure traces for all operating conditions are presented in Appendix B.

4.5.1. Effect of Speed

At a constant spark timing of 11.2°BTDC, measurements are taken at various speed conditions. Individual and average pressure traces of the engine are shown at 50% load and 350 RPM in Figure 22. At low load, the engine experiences frequent events of weak combustion, or partial combustion, where heat release occurs predominantly much later in the expansion stroke and only part of the fuel reaches products of complete combustion; this leads to higher CO and THC emissions, according to literature [23].

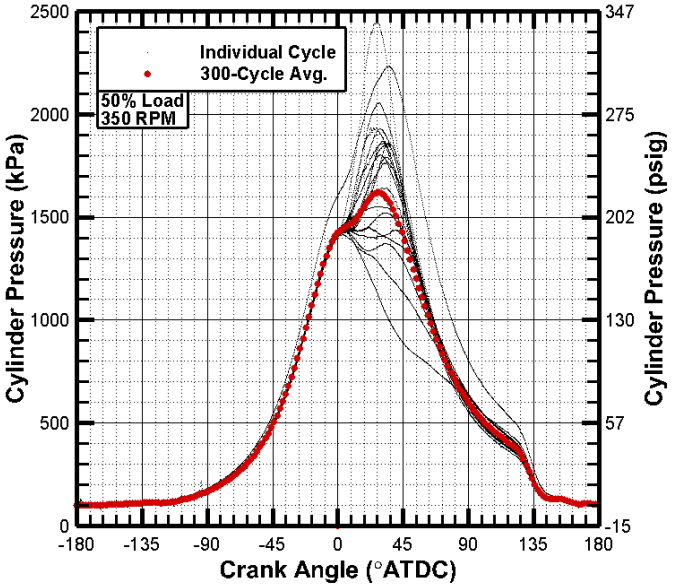

Figure 22. In-cylinder pressure data are shown for 20 non-sequential individual cycles and an average of 300 cycles for 50% load at 350 RPM.

One of the twenty non-sequential individually recorded cycles has higher pressure during the compression stroke and significantly higher pressure during the expansion stroke. This is likely due to strange scavenging behavior, since this type of engine is designed to operate mostly at high load. In a broader sense, since the engine is not designed to operate at lower load, operating points with low load conditions experience intense cyclic variation.

At the same load and at a speed of 400 RPM, the results change; the data are shown in Figure 23. At this operating point, one of the twenty non-sequential individually recorded cycles shows exceedingly delayed combustion, causing the cylinder pressure late in the expansion stroke to rise well above that of the other cycles. Another cycle is a simple misfiring curve, having no evidence of combustion. Again,

this could be due to improper scavenging at low load, causing a poorly prepared fuel-air mixture particularly around the spark plug.

In comparison with the low speed condition, this higher speed condition shows more cyclic variation. Partial burning cycles seem slightly more frequent, and misfiring cycles have been added where they were not previously present. This qualitatively confirms the COV of IMEP data discussed previously.

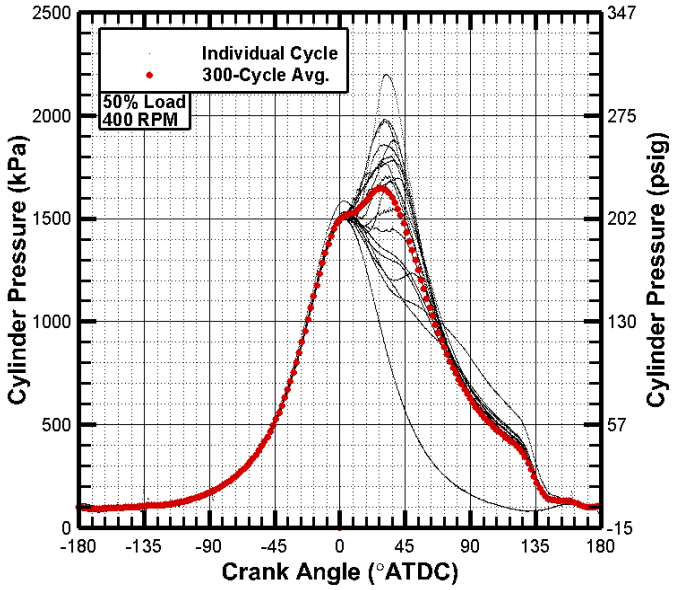

Figure 23. In-cylinder pressure data are shown for 20 non-sequential individual cycles and an average of 300 cycles for 50% load at 400 RPM.

The misfiring cycle provides a vantage point for further observations not necessarily related to the objective of the experiment. In an ideal misfiring curve of a two-stroke ported engine, the pressure at EPC should equal the pressure at EPO. In the data of the misfiring cycle, the pressure at EPC is 100 kPa_{abs}; at EPO the pressure has

decreased below atmospheric pressure to 89 kPa_{abs}. This could be due to a combination of blow-by around the piston rings and energy lost from heat transfer out of the cylinder. The misfiring cycle also shows the pressure noticeably rising after EPO, peaking at 130 kPa_{abs}. This is due to IPO, where the intake charge at a higher pressure begins to enter and equilibrate with the remaining gasses in the cylinder. The pressure then decreases to atmospheric pressure as equilibrium between the stuffing box, combustion chamber, and exhaust manifold is reached. In this process, gasses can exit the cylinder through the exhaust manifold; some of these gasses are short-circuiting the cylinder, going directly from the intake port to the exhaust port. It is this pressure differential that drives short-circuiting behavior and results in many of the emission behaviors previously discussed.

At a speed of 425 RPM, shown in Figure 24, the pressures at approximately 30°ATDC show an interesting, divergent or dual-mode behavior. In progression from 400 RPM to 425 RPM, cycles with quality combustion have higher peak pressures than those of quality combustion cycles at 400 RPM, with five cycles surpassing 2200 kPa_{abs} of peak pressure, and the cycle-averaged location of peak pressure seems to advance towards TDC in comparison with those at 400 RPM. Meanwhile, instances of partial combustion worsen, in comparison to those at 400 RPM, as the pressures between 0°ATDC and 60°ATDC are noticeably lower and decrease at a more rapid rate. This dual-mode behavior is due to two different modes of combustion occurring at the same operating condition [23, 48]. In one mode, specifically the one with retarded cycle-averaged locations of peak pressure, combustion occurs more quickly and thoroughly. Heat is released at a much faster rate than expansion work is leaving the cylinder. In the

other combustion mode, however, since combustion is slower, the rate of heat release is much slower, resulting in a lower peak pressure. The dual-mode behavior is simply an interesting manifestation from cyclic variation, which has continued to increase with increasing speed.

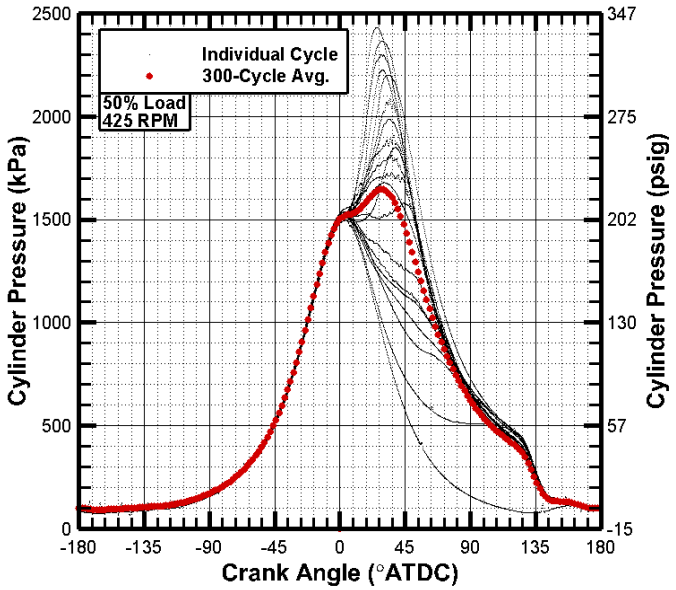

Figure 24. In-cylinder pressure data are shown for 20 non-sequential individual cycles and an average of 300 cycles for 50% load at 425 RPM.

Combustion appears to become more erratic at 475 RPM, shown in Figure 25A. Three of the twenty non sequential individually-recorded cycles are simple misfiring curves. One particular feature in Figure 25A is the two cycles that reach only 1460 kPa_{abs}, which is approximately 100 kPa below the other 18 cycles, so even the compression curves are different from cycle to cycle.

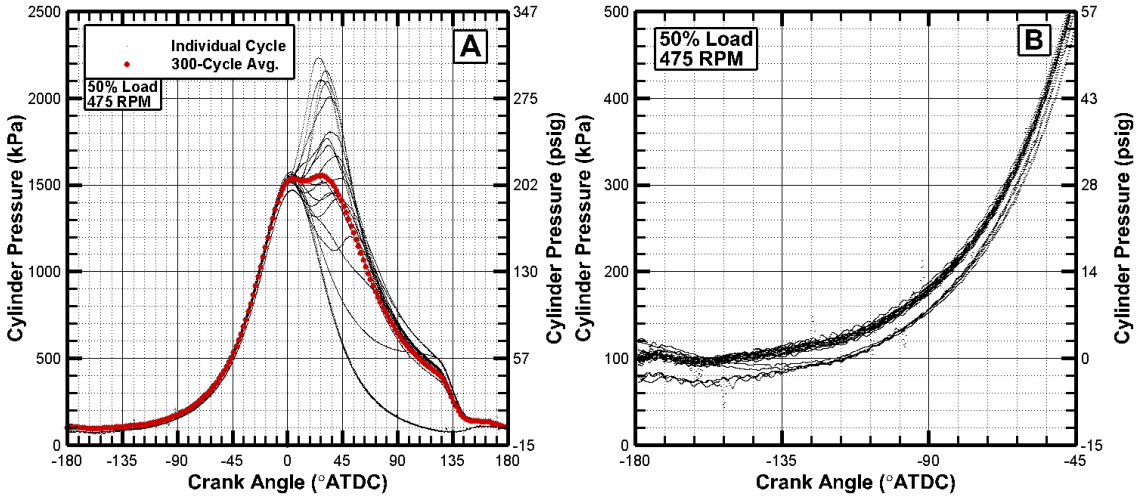

Figure 25. (A). In-cylinder pressure data are shown for 20 non-sequential individual cycles and an average of 300 cycles for 50% load at 475 RPM. (B). Detailed view of individually-recorded pressures before and after ports close prior to compression.

In the data shown in Figure 25, four cycles are 25 kPa lower than the average pressure. However, two of those cycles that have a lower pressure after EPC rejoin the compression curve of the other 16 cycles during the compression event. Perhaps these cycles have different heat transfer behavior. This would change the polytropic constant and lead to a different resulting pressure from the compression process, even though the initial pressure and the initial and final volumes are the same. Though the mechanism of this behavior is difficult to determine with certainty, this demonstrates the even greater degree of cyclic variation at this operating condition.

At 525 RPM, shown in Figure 26, combustion is most erratic. Three cycles demonstrate the lower compression curve, and one cycle misfires. This is the most apparently, or qualitatively, unstable operating condition in the test matrix, which

corresponds to the quantitative analysis of COV of IMEP. At the lowest load and highest speed, cyclic variation is greatest.

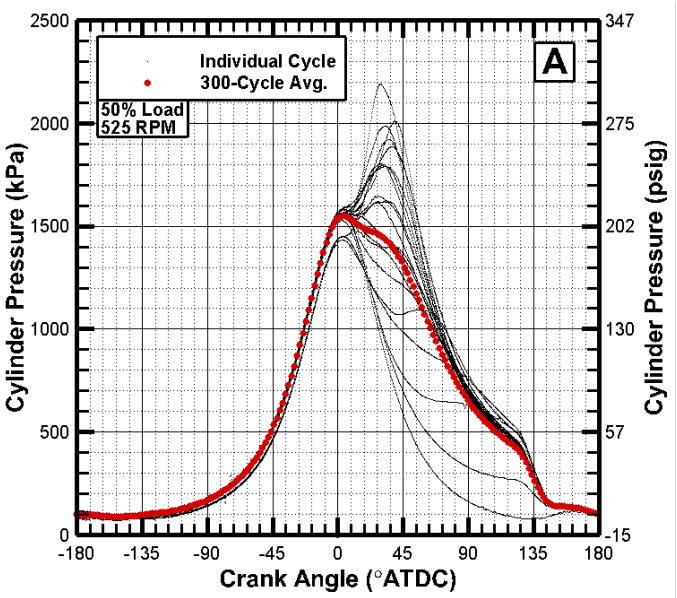

Figure 26. In-cylinder pressure data are shown for 20 non-sequential individual cycles and an average of 300 cycles for 50% load at 525 RPM.

At 93% load at 350 RPM, show in Figure 27, combustion shows strong signs of consistency. Compression and expansion curves are nearly identical on a cycle-to-cycle basis, while peak pressures range only between 3000 and 3600 kPa_{abs}. The pressure traces only noticeably differ cycle-by-cycle from approximately 0°ATDC to 30°ATDC.

At 93% load and 500 RPM, shown in Figure 28, the typical effects of speed are evident but diluted at this higher load. There is a slightly higher degree of cyclic variation, as peak pressures range between 1900 and 3300 kPa_{abs}, and pressure traces noticeably differ from approximately 0°ATDC to 45°ATDC. However, the compression

and expansion curves still show excellent agreement between the individual cycles, and there are no misfires or cycles with offset compression curves.

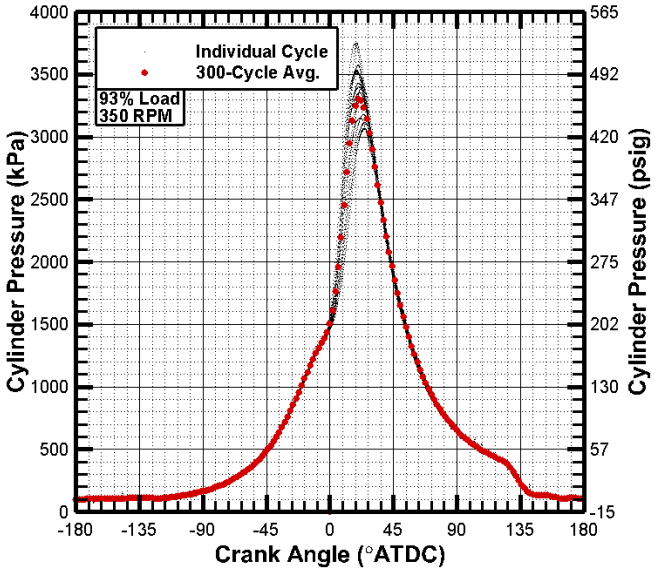

Figure 27. In-cylinder pressure data are shown for 20 non-sequential individual cycles and an average of 300 cycles for 93% load at 350 RPM.

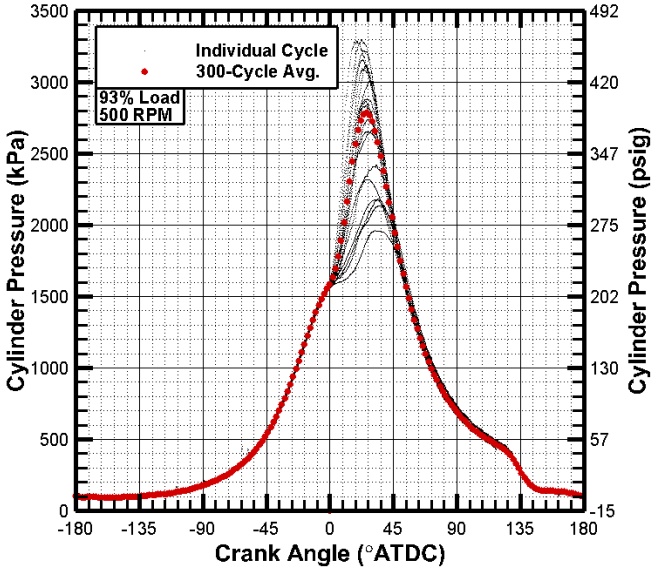

Figure 28. In-cylinder pressure data are shown for 20 non-sequential individual cycles and an average of 300 cycles for 93% load at 500 RPM.

In summary, at low load, combustion becomes increasingly erratic with increasing speed. Also at low load, the offset compression pressure phenomenon is present, shown in Figure 25, where the pressure at 0°ATDC is approximately 100 kPa lower than the motoring peak pressure. Again, this is a qualitative manifestation of the strange scavenging behavior existent at low load, which leads to high cyclic variation. Interestingly, all recorded instances of an offset compression pressure demonstrate partial combustion. Cylinder pressure during the expansion stroke varies significantly at operating conditions subject to high cyclic variation.

At very low speeds, 350-375RPM, there are no recorded misfires. At almost all other speeds, misfires occur at 50% and 63% load conditions. The absence of misfires at very low speeds could be a combination of better scavenging and a greater amount of time for the flame kernel to develop into a flame front. Interestingly, however, 500 RPM shows no misfires. This corresponds to the decrease in COV of IMEP in Figure 20.

4.5.2. Effect of Load

At a constant spark timing of 11.2°BTDC, measurements are taken at various load conditions. The effect of engine load is distinct when observing the in-cylinder pressure data. At 350 RPM, when increasing the load from 50%, shown in Figure 22, to 63%, shown in the Figure 29A, the apparent engine behavior drastically changes. Cyclic variation drastically decreases, as the cycles exhibiting partial burn are greatly reduced. Decrease in cyclic variation is quantitatively confirmed by the COV of IMEP results presented in Figure 8, and it leads to the more qualitatively cyclically consistent pressures in the higher load case, particularly noticeable during the expansion stroke.

While still at 350 RPM and increasing the load to 74%, shown in Figure 29B, the results continue much in the same way. The cyclic variation continues to improve. There are no clear individually recorded partial-burning cycles. The compression curves demonstrate an even higher degree of consistency. Pressure traces are noticeably different from TDC to approximately 65°ATDC in the 63% load case, while they are different from TDC to approximately only 45°ATDC in the 74% load condition. Again, this is qualitatively representing how increasing load decreases cyclic variation

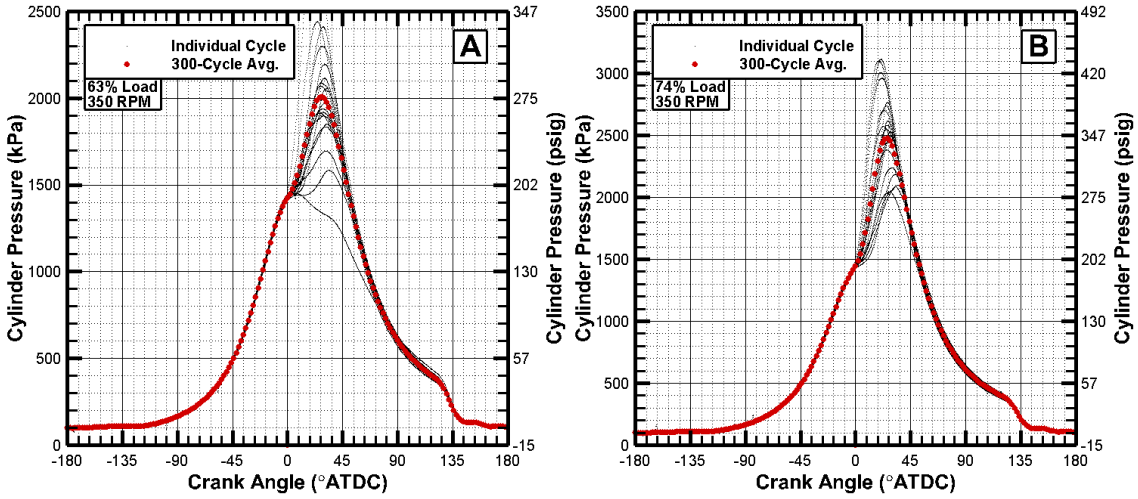

Figure 29. In-cylinder pressure data are shown for 20 non-sequential individual cycles and an average of 300 cycles for 350 RPM for (A) 63% load and (B) 74% load.

By increasing the load again to 93%, shown in Figure 27, combustion stability reaches a maximum as the COV of IMEP reaches a minimum in the tested operating conditions. This is evident in the apparent elimination of partial burn cycles and exceptional agreement in the non-sequential individually-recorded pressure traces.

Thus, by increasing load at a low speed of 350 RPM, cyclic variation was substantially decreased. The lowest COV of IMEP of all test conditions was attained at 350 RPM and 93% load. This is likely due to superior scavenging performance at these conditions.

This decreasing response of cyclic variation to an increasing load is then examined at a mid-range speed on the engine – 400 RPM. The in-cylinder pressure measurements at this speed and 50% load are shown in Figure 30A. When the load is then increased to 63%, shown in Figure 30B, several observations can once again be made. Again, the partial combustion events significantly improve; all cycles exhibiting combustion, less one, show a peak pressure that occurs after the motoring peak. Both the 50% and the 63% cases show a misfire occurring. Disregarding the misfiring cycles, the pressure traces in the 50% load case are noticeably different from TDC until blowdown, while they are different from TDC to approximately only 55°ATDC in the 63% load condition.

At a higher load of 93%, shown in Figure 31, the combustion stability continues to improve. Again, this is a qualitative observation confirmed by the COV of IMEP data presented in Figure 8. As a result, the expansion curves align much more consistently. At this load, no misfiring cycles are recorded.

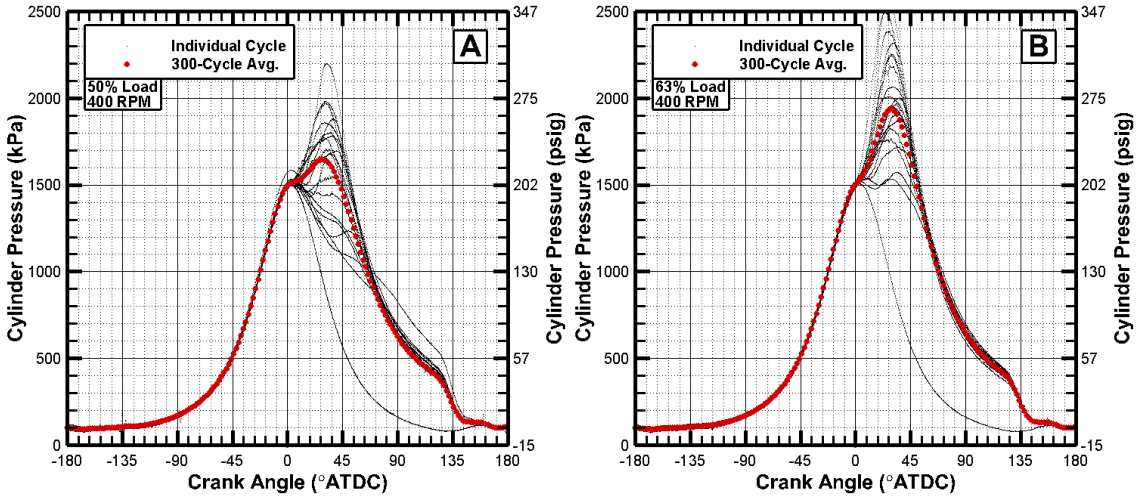

Figure 30. In-cylinder pressure data are shown for 20 non-sequential individual cycles and an average of 300 cycles for 4000 RPM for (A) 50% load and (B) 63% load.

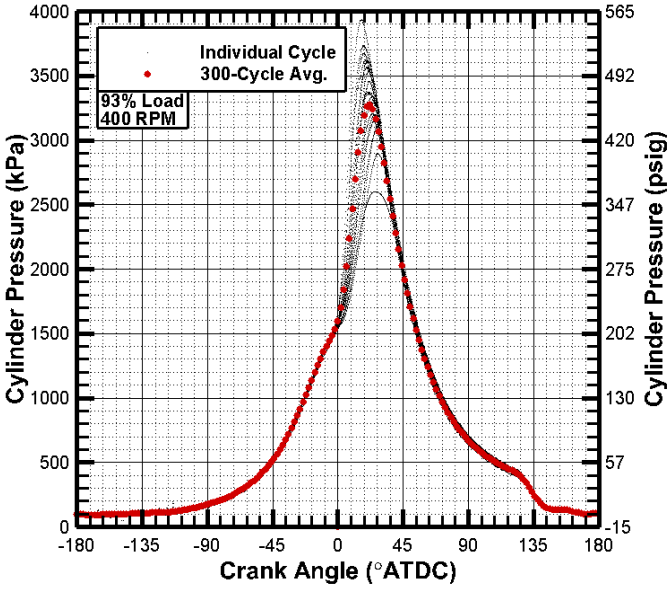

Figure 31. In-cylinder pressure data are shown for 20 non-sequential individual cycles and an average of 300 cycles for 93% load at 400 RPM.

The effect of increasing load on decreasing cyclic variation does not change at the highest engine speed of 525 RPM, shown in Figure 32. Increasing load from 63% to

100%, again, apparent combustion stability increases exceptionally. Misfiring cycles are eliminated. Cylinder pressure agreement is regained earlier towards TDC after peak pressure variance.

Thus, in general, increasing engine load dramatically increases engine stability. Non sequential individually recorded cycles exhibiting compression pressure offset phenomenon are eliminated at and above 74% load. Recorded misfiring cycles, except for the operating point of 525 RPM and 74% load, are eliminated at and above 74% load. Exhaust stroke pressure traces are more cyclically consistent as well.

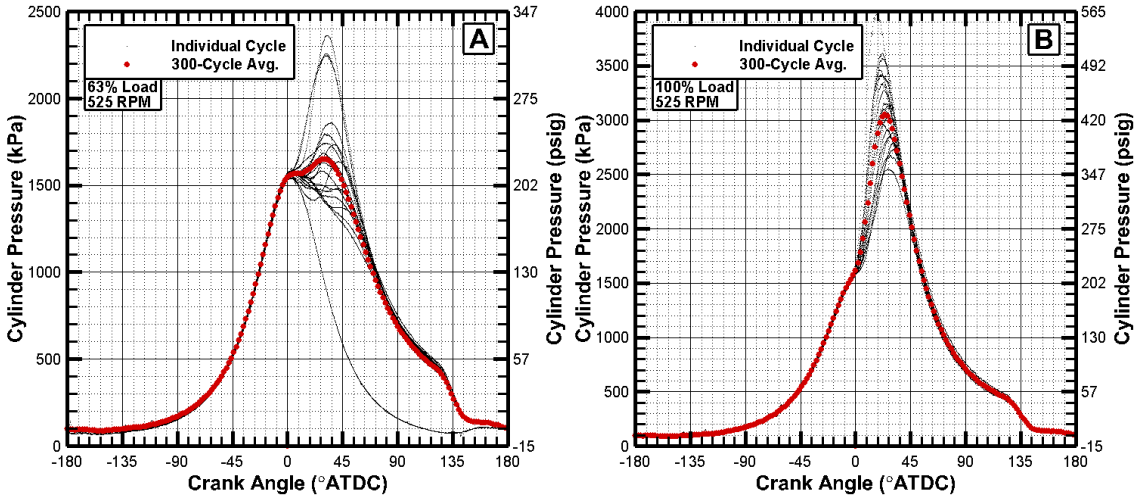

Figure 32. In-cylinder pressure data are shown for 20 non-sequential individual cycles and an average of 300 cycles for 525 RPM at (A) 63% load and (B) 100% load.

5. SUMMARY AND CONCLUSIONS

This study quantifies and describes within the context of cyclic variation the behavior of the following engine parameters as functions of speed and load: in-cylinder pressure, COV of IMEP, air flow rate, equivalence ratio, delivery ratio, air and fuel trapping efficiencies, and emissions.

In-cylinder pressure, at low load, shows increasing COV of IMEP with increasing speed; the engine is approximately twice more stable at low speeds than at high speeds. Also at low load, the offset compression pressure phenomenon is present, where the pressure at 0°ATDC is approximately 100 kPa lower than the motoring peak pressure, shown in Figure 25. This is likely a manifestation of poor scavenging behavior related to high cyclic variation at this condition. Cylinder pressure during the expansion stroke cyclically varies significantly at operating conditions subject to high COV of IMEP. At very low speeds, there are no recorded misfires. Generally, misfires occur at low load and high speed conditions. Both of these observations trend with cyclic variation as well. The finding of increasing cyclic variation with increasing speed agrees with the predictions presented in Chapter 2, and are likely a result of stronger turbulence inhibiting flame kernel growth.

In general, increasing engine load dramatically increases engine stability by decreasing the COV of IMEP; the engine is an order of magnitude more stable at full load than at half load. This agrees with the predicted trend presented in Chapter 2, and could be a result of better scavenging, specifically near the spark plug. Individually recorded cycles exhibiting compression pressure offset phenomenon are eliminated at

and above 74% load. Recorded misfiring cycles are all but eliminated at and above 74% load. Exhaust stroke pressure traces are more cyclically consistent as well.

The data shows an increase in the air flow rate as a function of speed. This is likely due to the greater number of intake events in the engine. Though these comments can be made for speed, no statistically meaningful observations can be made regarding the impact of load on air flow rate.

Equivalence ratio data show an increase with increasing load and a decrease with increasing speed, with values between 0.55 and 0.90. BSFC trends as functions of speed or load are impossible to state with 95% confidence, though a decrease with increasing load is suggested by the data.

The average delivery ratio is over 1.0 at most operating conditions. This likely suggests a loss of mass in the cylinder due to short-circuiting behavior. Also, the delivery ratio at 350 RPM is between 0.45 and 1.55; the delivery ratio at 525 RPM is between 0.85 and 1.75. Since trends cannot be made with respect to speed or load, however, correlation with cyclic variation is difficult.

Fuel trapping efficiency increases as speed increases from 350 to 375 RPM, decreases as speed increases to 500 RPM, and then increases slightly as speed further increases to 525 RPM. This matches a trend found by Blair and Kenny. Also, the generally decreasing trend of trapping efficiency correlates well with the generally increasing trend of delivery ratio with increasing speed; this trend is also confirmed by Blair and Kenny's study. Values range between 35% and 42%.

Air trapping efficiency values range between 19% and 32%. The fact that these trapping efficiencies disagree notably with the fuel trapping efficiencies suggests that one or both of the datasets are incorrect. The air trapping efficiency dataset could be the culprit. The use of Equation (17) is discouraged in lean-burning engines, and the overall system equivalence ratio of the engine suggests the engine used in this study is indeed lean-burning. Scavenging efficiency, calculated using trapping efficiency, is therefore not credible. Values are above 100%, which is not possible. These discrepancies serve as future work, as improvement to these data requires modification of the fuel system.

The effect of speed on CO emissions is difficult to determine with certainty. Increasing load, however, causes a decrease in CO emissions. This trends with decreasing cyclic variation, which decreases partial combustion behavior, and it agrees with expectations of literature presented in Chapter 2. Also, as cyclic variation decreases with increasing load, CO_2 increases, indicating greater combustion efficiency. Additionally, since the CO_2 emissions trend decreasingly with speed, CO emissions could be suspected to increase with increasing speed. This would correlate well with cyclic variation; as it increases with increasing speed, more frequent events of partial burn could elevate CO levels. Though this would disagree with an expectation from literature, the experiment used to set forth this expectation used engine speeds an order of magnitude higher than those in the present study. This disagreement, therefore, is acceptable.

At all tested loads, increasing the speed from 350 RPM to 400 RPM causes THC emissions decrease. This agrees with the literature presented in Chapter 2. Also, THC emissions noticeably increase with increasing load.

O_2 concentration decreases with increasing load. This is likely due to the apparent decrease in cyclic variation. Concentration of O_2 also shows dependence on speed, generally increasing with increasing speed, which trends with the decreasing equivalence ratio. This is likely due to the increased cyclic variation at higher speeds, where partially-burning cycles would leave O_2 unburned or misfiring cycles would leave all of the O_2 unburned.

At low load, NO production is low. This could be a result of poor scavenging, which would result in a higher residual fraction and serve as a crude form of EGR; this correlates with increasing cyclic variation as load decreases. At loads at and above 84%, a clear trend emerges where NO production decreases with increasing speed. Again, this correlates with increasing cyclic variation, which could be increasing the exhaust residuals because of worsening scavenging.

For CH_4, the statistical uncertainty on the measurements that were made within the range of the analyzer is high, making a trend with respect to speed impossible to determine with confidence. CH_4 emissions increase with increasing load. CH_4 emissions cannot comprise less than 80% of the THC emissions at loads at or lower than 63%, and they cannot comprise less than 57% of THC emissions at loads at or higher than 74%.

Emissions of CO_2, NO, and THC are shown (and emissions of CH_4 are suspected) to have an inverse correlation with cyclic variation; emissions of O_2 are shown (and emissions of CO are suspected) to have direct correlation with cyclic variation.

REFERENCES

1. Ferrara, G., Balduzzi, F., and Vichi, G., "An Innovative Solution for Two-Stroke Engines to Reduce the Short-Circuit Effects," SAE Technical Paper 2012-01-0180, 2012, doi:10.4271/2012-01-0180.

2. Abraham, M. and Prakash, S., "A Theory of Cyclic Variations in Small Two-Stroke Cycle Spark Ignited Engines - An Analytical Validation of Experimentally Observed Behaviour," SAE Technical Paper 920426, 1992, doi:10.4271/920426.

3. Daily, J., "Cycle-To-Cycle Variations: A Chaotic Process?," SAE Technical Paper 870165, 1987, doi:10.4271/870165.

4. Young, M., "Cyclic Dispersion – Some Quantitative Cause-and-Effect Relationships," SAE Technical Paper 800459, 1980, doi:10.4271/800459.

5. Winsor, R. and Patterson, D., "Mixture Turbulence - A Key to Cyclic Combustion Variation," SAE Technical Paper 730086, 1973, doi:10.4271/730086.

6. Peters, B. and Borman, G., "Cyclic Variations and Average Burning Rates in a S. I. Engine," SAE Technical Paper 700064, 1970, doi:10.4271/700064.

7. Matekunas, F., "Modes and Measures of Cyclic Combustion Variability," SAE Technical Paper 830337, 1983, doi:10.4271/830337.

8. Hi11, P., "Cyclic Variation and Turbulence Structure on Spark Ignition Engines." Combustion & Flame, April, 1988.

9. Karim, G., "An Examination of the Nature of the Random Cyclic Pressure Variations in a Spark-Ignited Engine." *Journal of the Institute of Petroleum*. Vo1. 53, No. 519, pp. 112-120, 1967.

10. Barton, R., Kenemuth, D., Lestz, S., and Meyer, W., "Cycle-by-Cycle Variations of a Spark Ignition Engine - A Statistical Analysis," SAE Technical Paper 700488, 1970, doi:10.4271/700488.

11. Hansel, J., "Lean Automotive Engine Operation - Hydrocarbon Exhaust Emissions and Combustion Characteristics," SAE Technical Paper 710164, 1971, doi:10.4271/710164.

12. Quader, A., "What Limits Lean Operation in Spark Ignition Engines-Flame Initiation or Propagation?" SAE Technical Paper 760760, 1976, doi:10.4271/760760.

13. Young, M., "Cyclic Dispersion in the Homogeneous-Charge Spark-Ignition Engine – A Literature Survey," SAE Technical Paper 810020, 1981, doi:10.4271/810020.

14. Mavropoulos, G., Rakopoulos, C., and Hountalas, D., "Experimental Assessment of Instantaneous Heat Transfer in the Combustion Chamber and Exhaust Manifold Walls of Air-Cooled Direct Injection Diesel Engine", *SAE International Journal of Engines*. Vol. 1, No. 1, pp. 888-912, 2009, doi:10.4271/2008-01-1326.

15. Uludogan, A., Foster, D., and Reitz, R., "Modeling the Effect of Engine Speed on the Combustion Process and Emissions in a DI Diesel Engine," SAE Technical Paper 962056, 1996, doi:10.4271/962056.

16. Caton, J., "Comparisons of Thermocouple, Time-Averaged and Mass-Averaged Exhaust Gas Temperatures for a Spark-Ignited Engine", SAE Technical Paper 820050, 1982, DOI: 10.4271/820050.

17. Heywood, J., Higgins, J., and Watts, P., "Development and Use of a Cycle Simulation to Predict SI Engine Efficiency and NOx Emissions", SAE Technical Paper 790291, 1979, DOI: 10.4271/790291.

18. Sawada, T., Wada, M., Noguchi, M., and Kobayashi, B., ""Development of a Low Emission Two-Stroke Cycle Engine," SAE Paper 980761, 1998, DOI: 10.4271/980761.

19. Duret, P., Venturi, S., and Carey, C., "The IAPAC Fluid Dynamically Controlled Automotive Two-Stroke Combustion Process – A New Generation of Two-Stroke Engines for the Future?" pp. 77-98, Proceedings of the International Seminar held at IFP, Rueil-Malmai son, France, Nov. 29-30, Editions Technip, Paris, 1993.

20. Abthoff, J., Duvinage, F., Hardt, T., Kramer, M., and Paule, M., "The 2-Stroke DI Diesel Engine with Common Rail Injection for Passenger Car Application," SAE Paper 981032, 1998, DOI: 10.4271/981032.

21. Nomura, K., and Nakamura, N., "Development of a New Two-Stroke Engine with Poppet-Valves: Toyota S-2 Engine – *A New Generation of Two-Stroke Engines for the Future?*" pp. 53-62, Proceedings of the International Seminar held at IFP, Rueil-Malmaison, France, Nov. 29-30, Editions Technip, Paris, 1993.

22. Kumar, P., "Significance of the Ratio of Exhaust Temperature to Coolant Temperature and Its Effect on Various Engine Working Parameters,"

Proceedings of the World Congress on Engineering held at London, U.K., Jul. 1-3, 2009.

23. Heywood, J. and Sher, E., *The Two-Stroke Cycle Engine*, Taylor & Francis, ISBN: 1-56032-831-2, Philadelphia, Pennsylvania, 1989.

24. "Description of AJAX Engines." Cameron Corporation: AJAX Products Group.

25. Gas Analysis Report. (2015, March 3). Hicks Dry Plant. Retrieved April 28, 2015, from Atmos Energy Corporation.

26. Principle of eddy-current electro brake dynamometer. Retrieved January 16, 2015, from http://www.tokyometer.co.jp/product1/dyna/cat12_6e.htm

27. User manual: NI 9752. (2013). Retrieved January 20, 2015, from http://www.ni.com/pdf/manuals/376101a.pdf

28. Operating instructions and specifications: NI 9205. (2008). Retrieved January 20, 2015, from http://www.ni.com/pdf/manuals/374188d.pdf

29. Lancaster, D., Krieger, R., and Lienesch, J., "Measurement and analysis of engine pressure data" SAE Technical Paper 750026, 1975, DOI: 10.4271/750026.

30. Kim, K., and Kim, S., "Measurement of Dynamic TDC in SI Engines Using Microwave Sensor, Proximity Probe and Pressure Transducers" SAE Technical Paper 891823, 1989, DOI: 10.4271/891823.

31. Pipitone, E., Beccari, A., and Beccari, S., "Reliable TDC Position Determination: A Comparison of Different Thermodynamic Methods through Experimental Data and Simulations" SAE Technical Paper 2008-36-0059, 2008, DOI: 10.4271/2008-36-0059.

32. Thomas, D. and Culmer, J., "Laminar Flow Elements." *Flow Control*, 2001, Vol. 7, No. 3, pp. 34-36.

33. Beckwith, T., Marangoni, R., and Lienhard, J., *Mechanical Measurements*, Pearson Prentice Hall, ISBN: 0201847655, Upper Saddle River, New Jersey, 2007.

34. Kline, S., and McClintock, F., 1953, "Describing Uncertainties in Single-Sample Experiments," Mechanical Engineering, Vol. 75, Jan., pp. 3-8.

35. Laminar Flow Elements – Installation and Operating Instructions. (2014, March 7). Meriam Process Technologies.

36. Blair, G., *Design and Simulation of Two-Stroke Engines*, Society of Automotive Engineers, Inc., ISBN: 1-56091-685-0, Warrendale, Pennsylvania, 1996.

37. Mashayekh, A., and Jacobs, T., "CFD Framework for the Study of Conjugate Heat Transfer of a Spark-Ignited Natural Gas Engine Cylinder." ASME 2015 ICEF Technical Conference. Under Review.

38. Heywood, J. and Holman, J., *Internal Combustion Engine Fundamentals*, McGraw-Hill, Inc., ISBN: 0-07-028637-X, New York City, New York, 1988.

39. A. Polk, personal communication, June 1, 2015.

40. Mackenzie, F. and Mackenzie, J. (1995) *Our Changing Planet*. Prentice-Hall, ISBN: 0-32166-772-7, Upper Saddle River, NJ, p 288-307.

41. Friedli, H., Lötscher, H., Oeschger H., Siegenthaler, U. and Stauffer, B. 1986. "Ice core record of 13C/12C ratio of atmospheric CO2 in the past two centuries." Nature 324:237--238.

42. Matekunas, F., "Modes and Measures of Cyclic Combustion Variability," SAE Technical Paper 830337, 1983, DOI:10.4271/830337.

43. Hurley, T., "E-565 Performance Test Results," Report (April 21, 2011). GE: Oklahoma City, Oklahoma.

44. Blair, G., and Kenny, R., "Futher Developments in Scavenging Analysis for Two-Cycle Engines," SAE paper 800038, 1980, DOI: 10.4271/800038.

45. Jun, D., Ishii, K., and Iida, N., "Combustion Analysis of Natural Gas in a Four Stroke HCCI Engine Using Experiment and Elementary Reactions Calculation," SAE Technical Paper 2003-01-1089, 2003, DOI: 10.4271/2003-01-1089.

46. Harrington, J., and Shishu, R., "A Single-Cylinder Engine Study of the Effects of Fuel Type, Fuel Stoichiometry and Hydrogen-to-Carbon Ratio on CO, NO, and HC Exhaust Emissions," SAE paper 730476, 1973, DOI: 10.4271/730476.

47. Stivender, D., "Development of a Fuel-Based Mass Emission Measurement Procedure," SAE paper 710604, 1971, DOI: 10.4271/710604.

48. Miles, P., Green, R., and Witze, P., "In-Cylinder Gas Velocity Measurements Comparing Crankcase and Blower Scavenging in a Fired Two-Stroke Cycle Engine," SAE paper 940401, 1994, DOI: 10.4271/940401.

APPENDIX A

LINEARITY TEST RESULTS

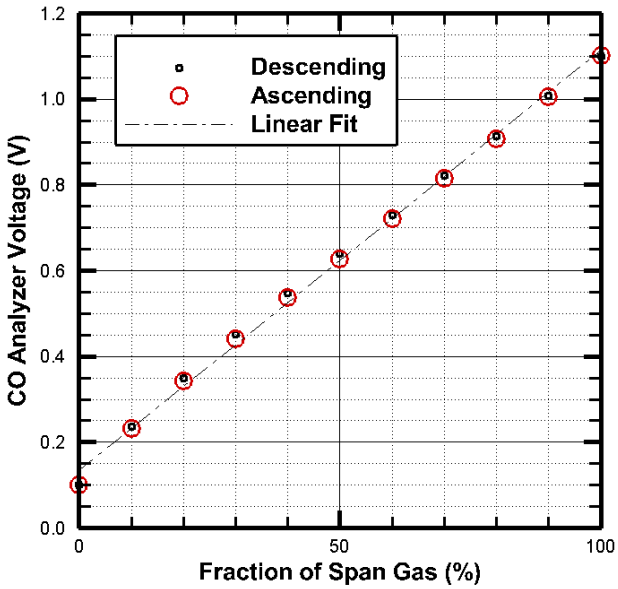

Figure A- 1. Linearity of CO analyzer from the emissions bench in 5,000 ppm range.

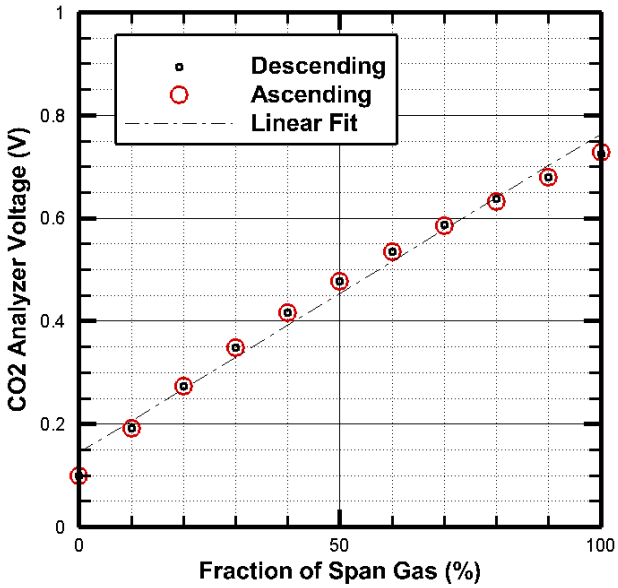

Figure A- 2. Linearity of CO_2 analyzer from the emissions bench in 80,000 ppm range.

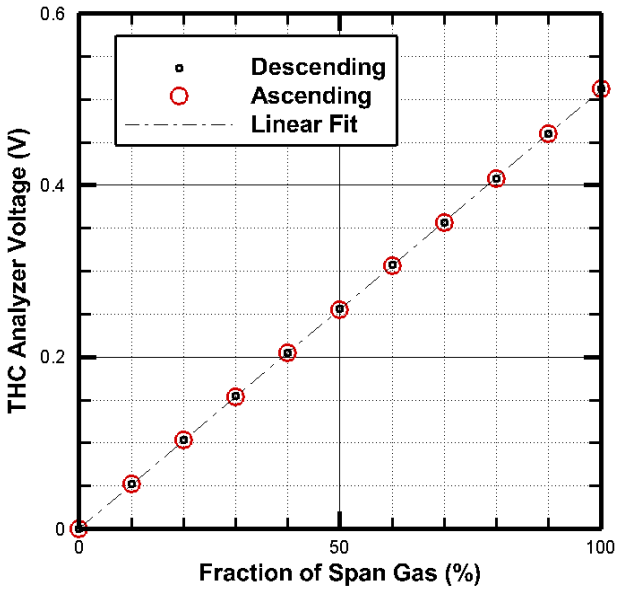

Figure A- 3. Linearity of THC analyzer from the emissions bench in 10,000 ppm range.

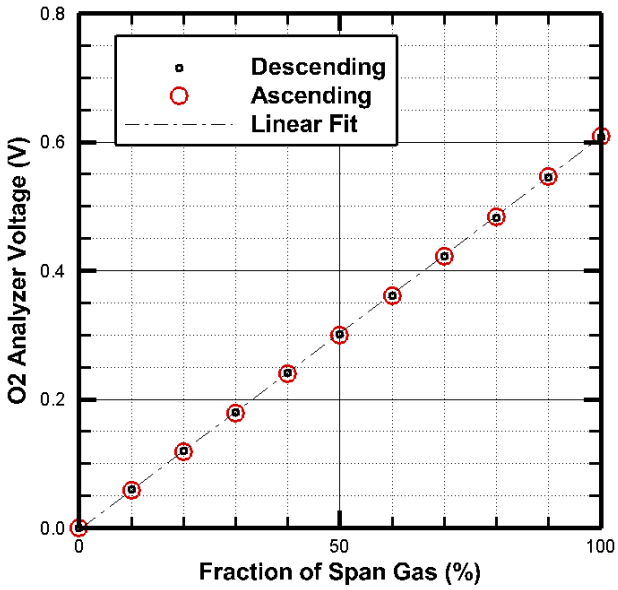

Figure A- 4. Linearity of O_2 analyzer from the emissions bench in 250,000 ppm range.

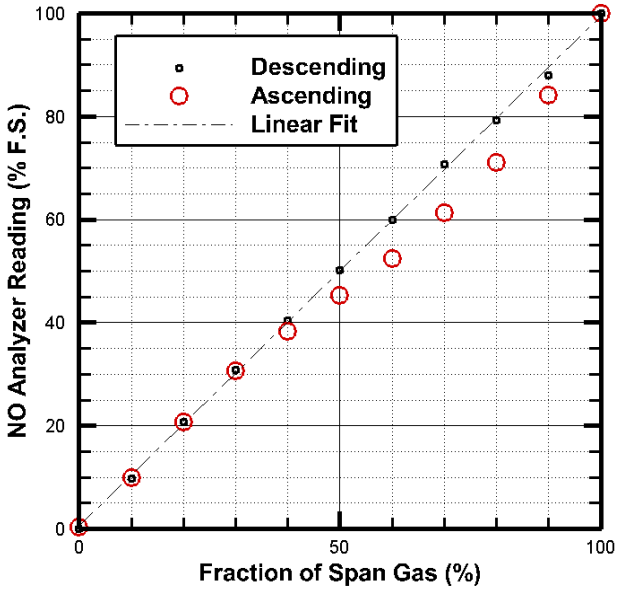

Figure A- 5. Linearity of NO analyzer from the emissions bench in 1,000 ppm range.

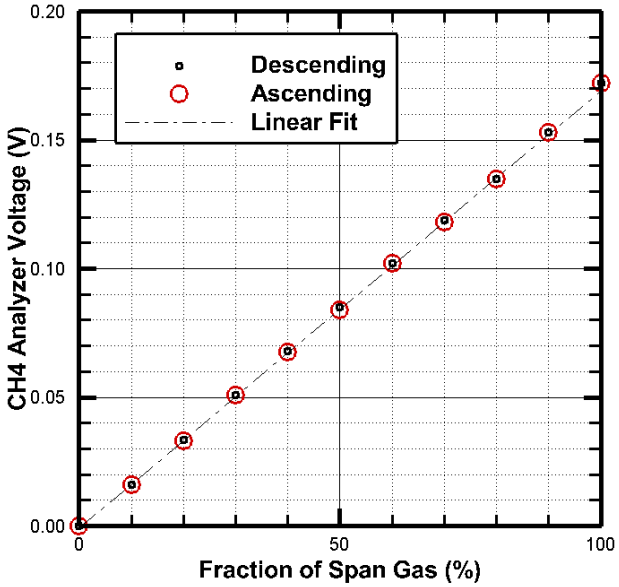

Figure A- 6. Linearity of CH_4 analyzer from the emissions bench in 30,000 ppm range.

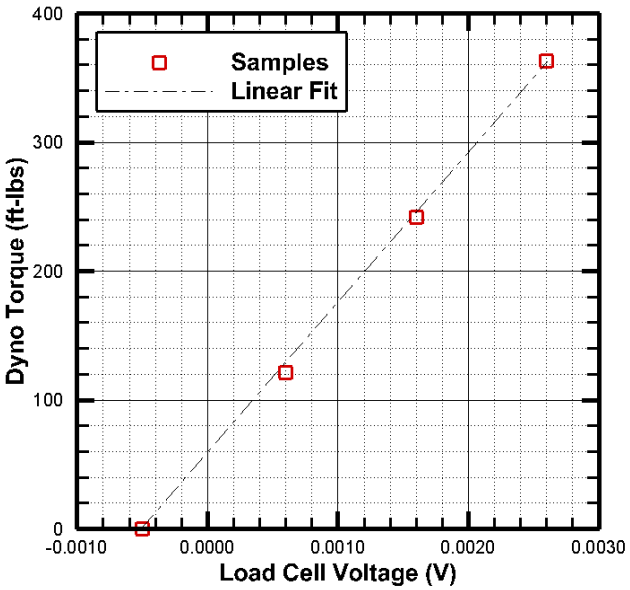

Figure A- 7. Linearity of load cell on dynamometer.

APPENDIX B

INDIVIDUAL CYCLE DATA

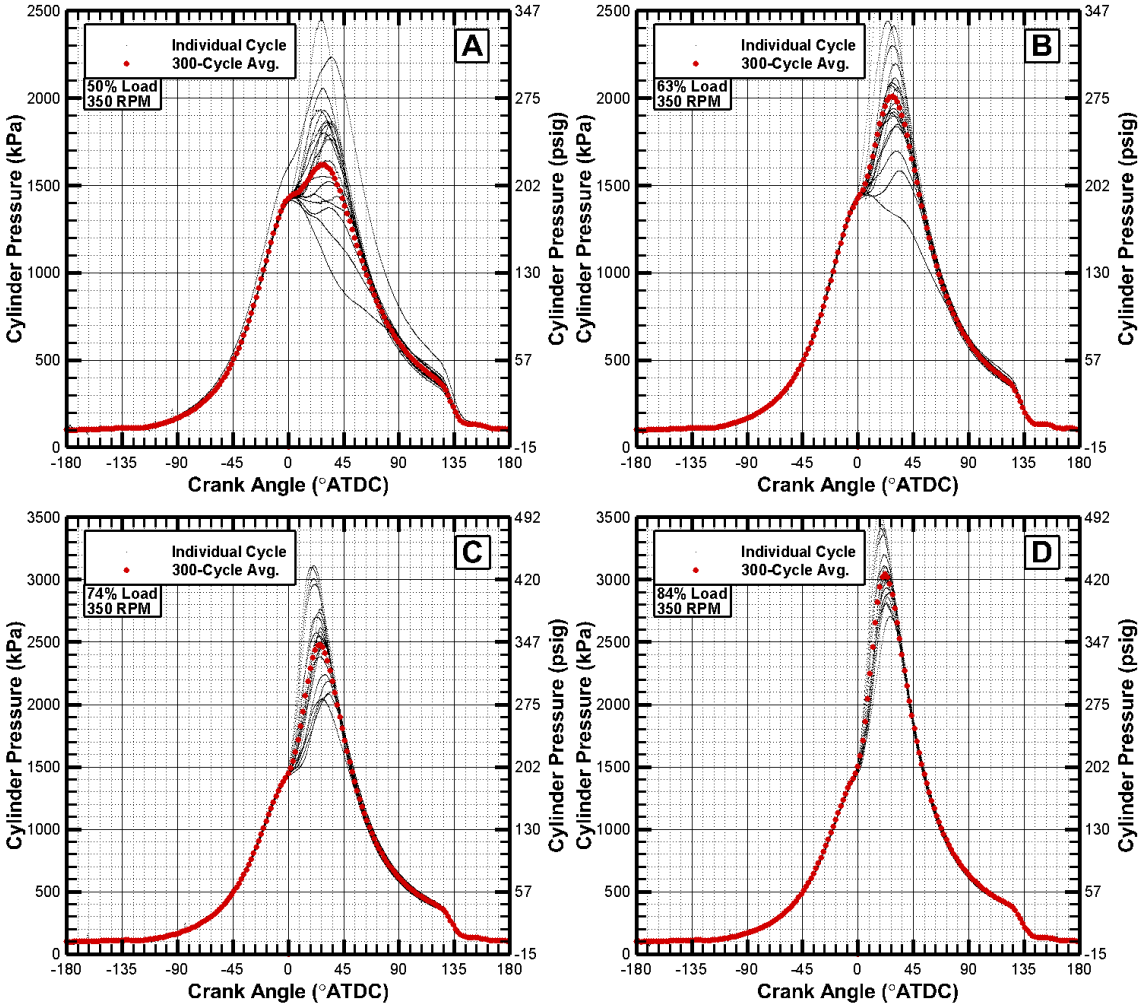

Figure B- 1. Twenty individual cycles and 300-cycle averaged in-cylinder pressure measurements are shown as a function of crank angle at 350 RPM for A) 50% load, B) 63% load, C) 74% load, D) 84% load, and E) 93% load.

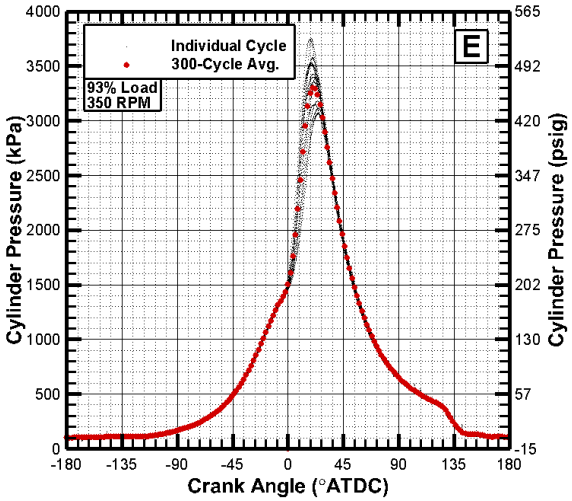

Figure B- 1. Continued.

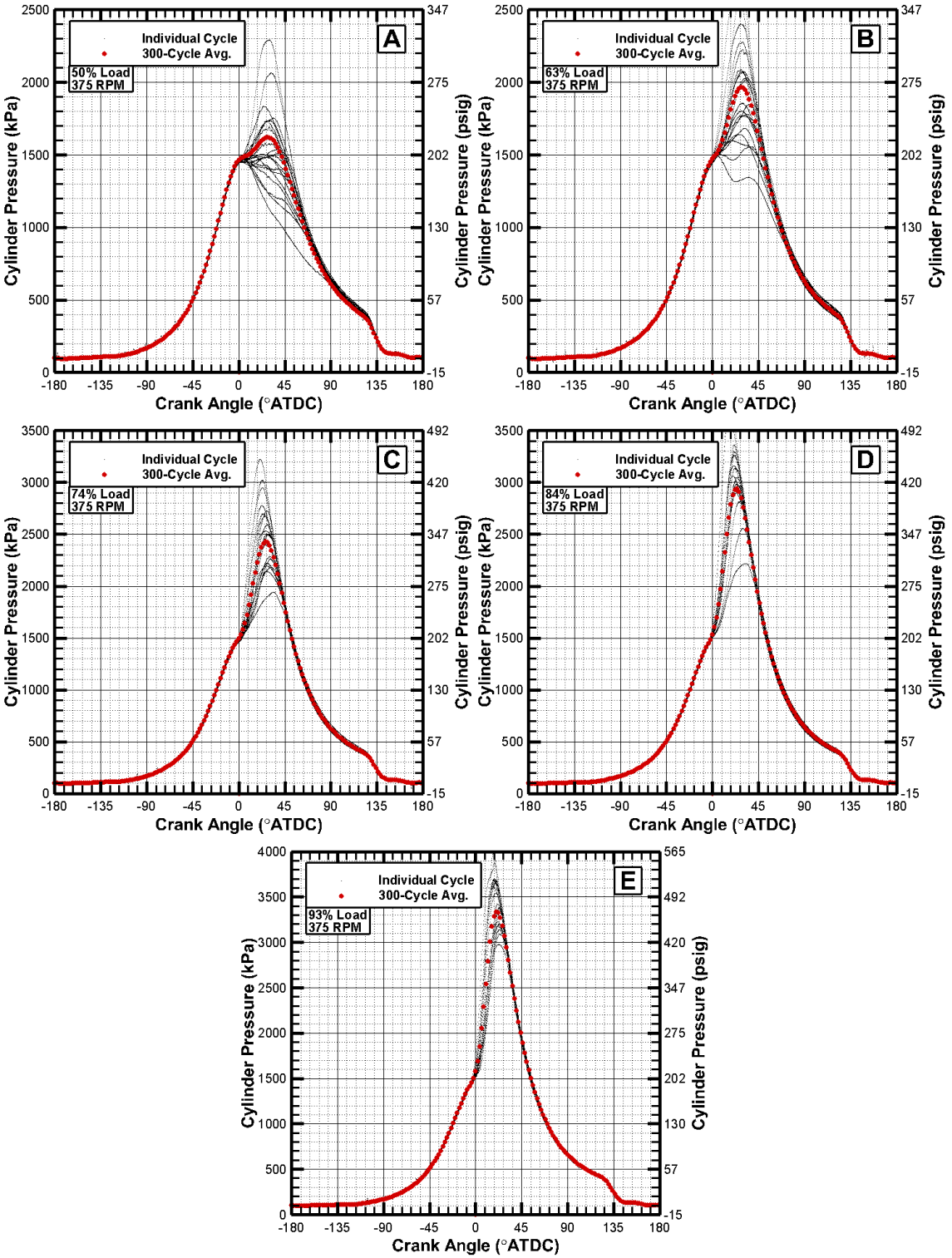

Figure B- 2. Twenty non-sequential individual cycles and 300-cycle averaged in-cylinder pressure measurements are shown as a function of crank angle at 375 RPM for A) 50% load, B) 63% load, C) 74% load, D) 84% load, and E) 93% load.

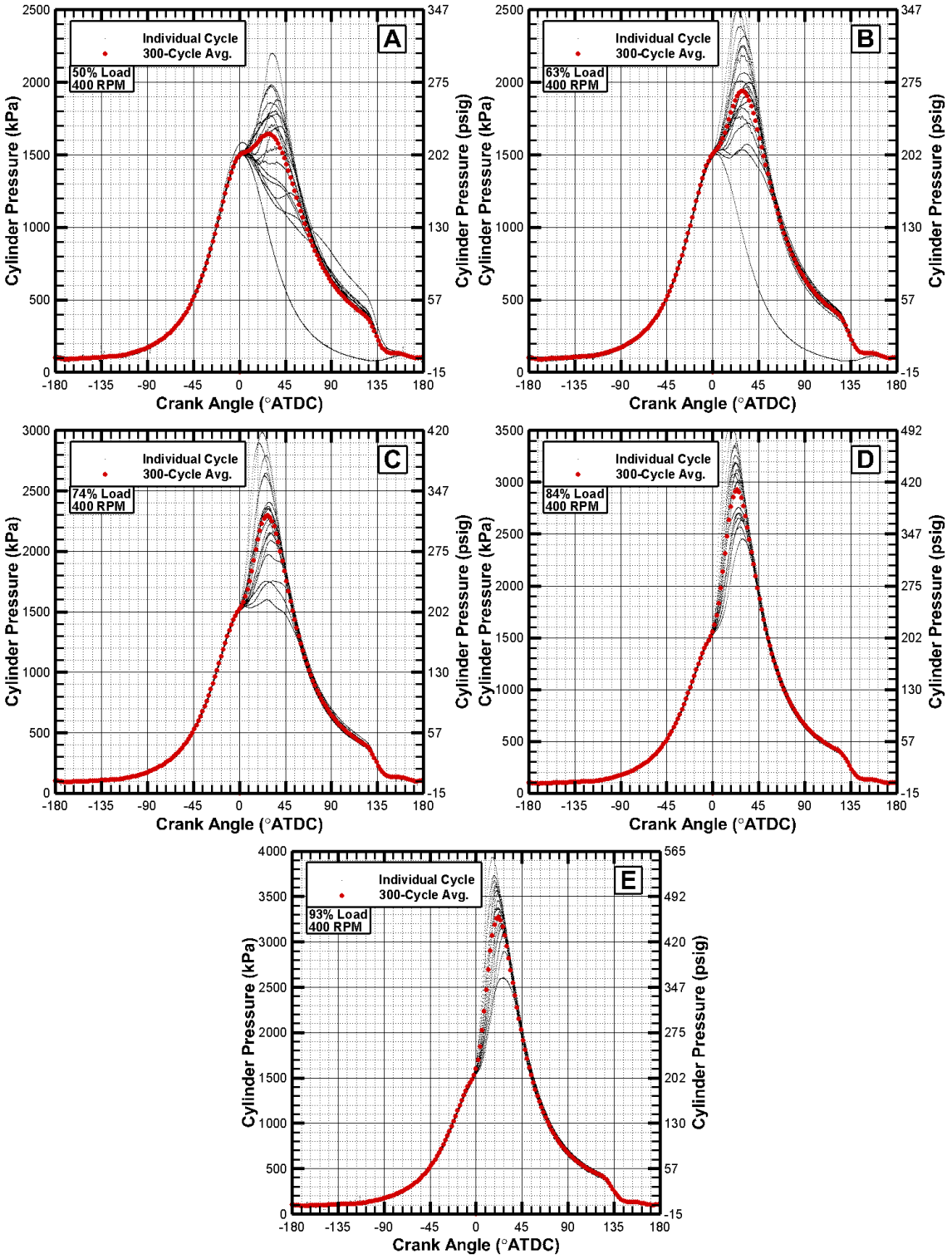

Figure B- 3. Twenty non-sequential individual cycles and 300-cycle averaged in-cylinder pressure measurements are shown as a function of crank angle at 400 RPM for A) 50% load, B) 63% load, C) 74% load, D) 84% load, and E) 93% load.

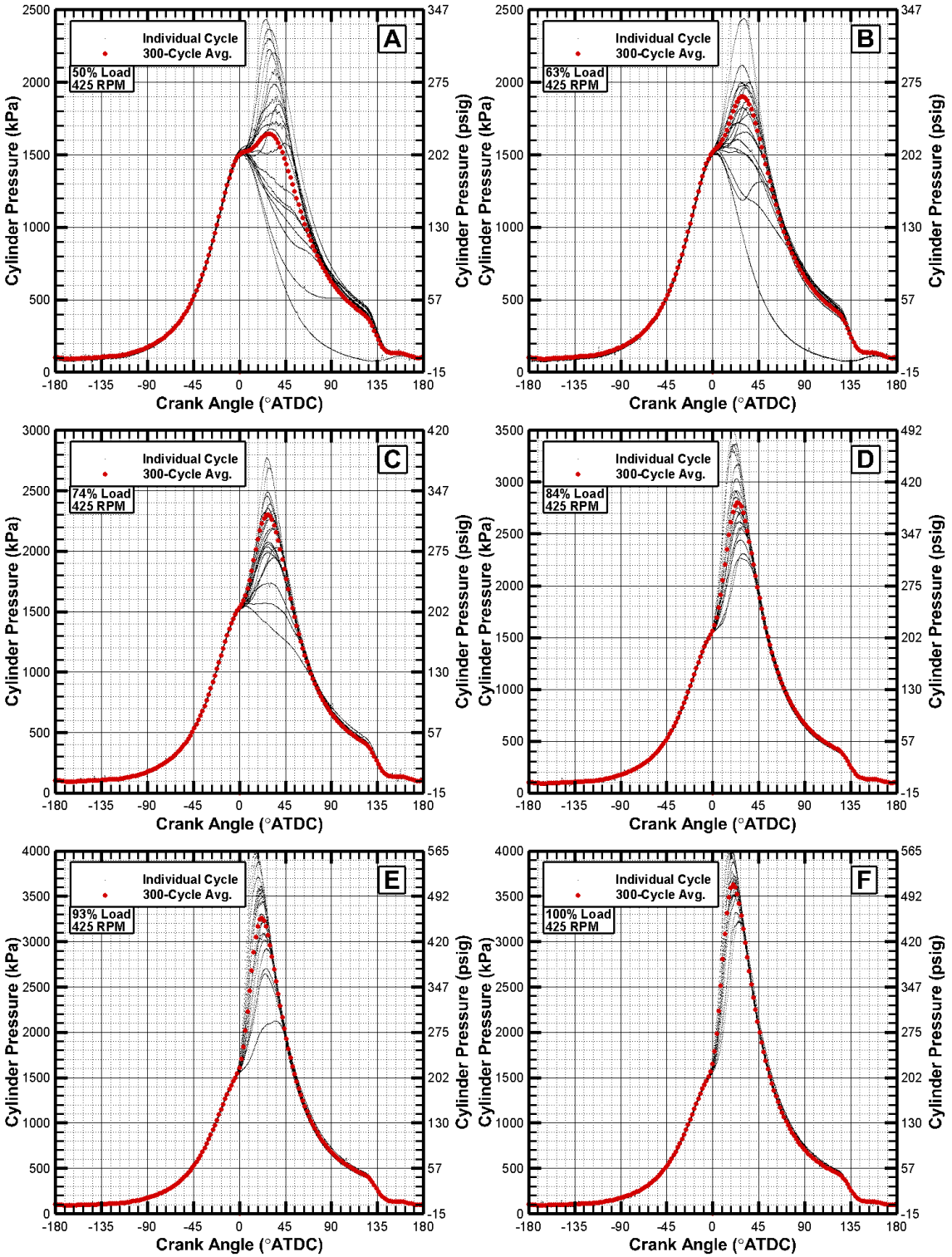

Figure B- 4. Twenty non-sequential individual cycles and 300-cycle averaged in-cylinder pressure measurements are shown as a function of crank angle at 425 RPM for A) 50% load, B) 63% load, C) 74% load, D) 84% load, E) 93% load, and F) 100% load.

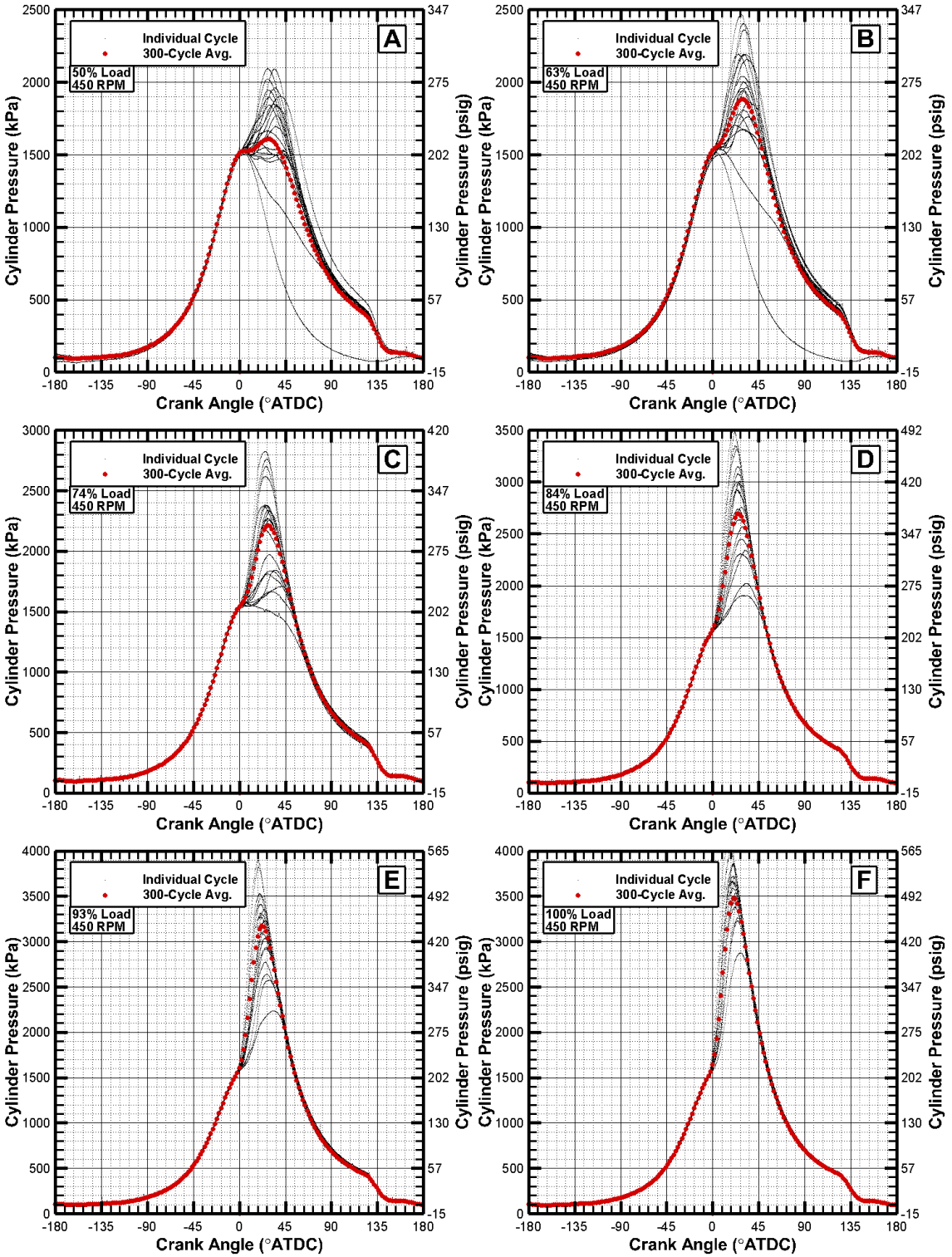

Figure B- 5. Twenty non-sequential individual cycles and 300-cycle averaged in-cylinder pressure measurements are shown as a function of crank angle at 450 RPM for A) 50% load, B) 63% load, C) 74% load, D) 84% load, E) 93% load, and F) 100% load.

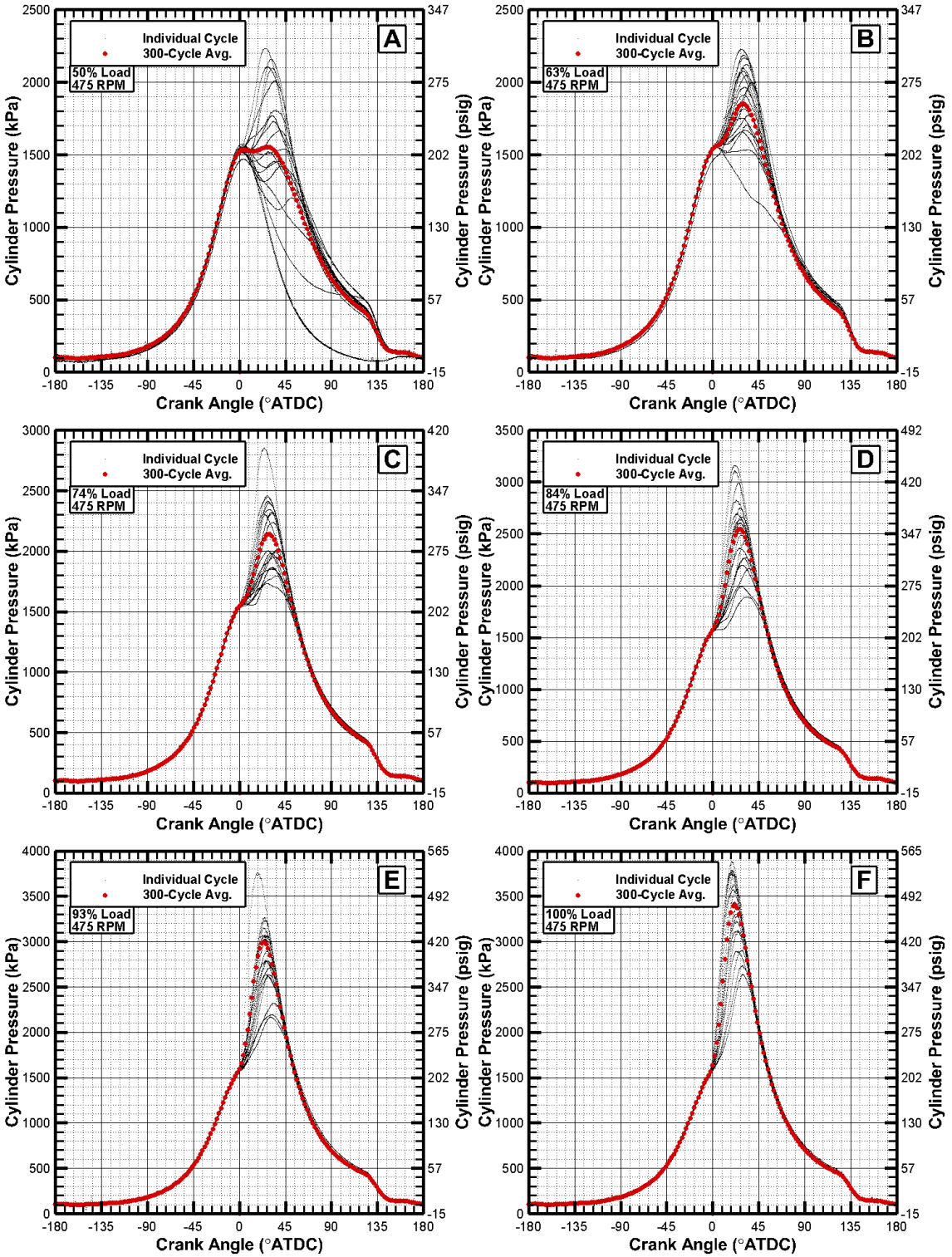

Figure B- 6. Twenty non-sequential individual cycles and 300-cycle averaged in-cylinder pressure measurements are shown as a function of crank angle at 475 RPM for A) 50% load, B) 63% load, C) 74% load, D) 84% load, E) 93% load, and F) 100% load.

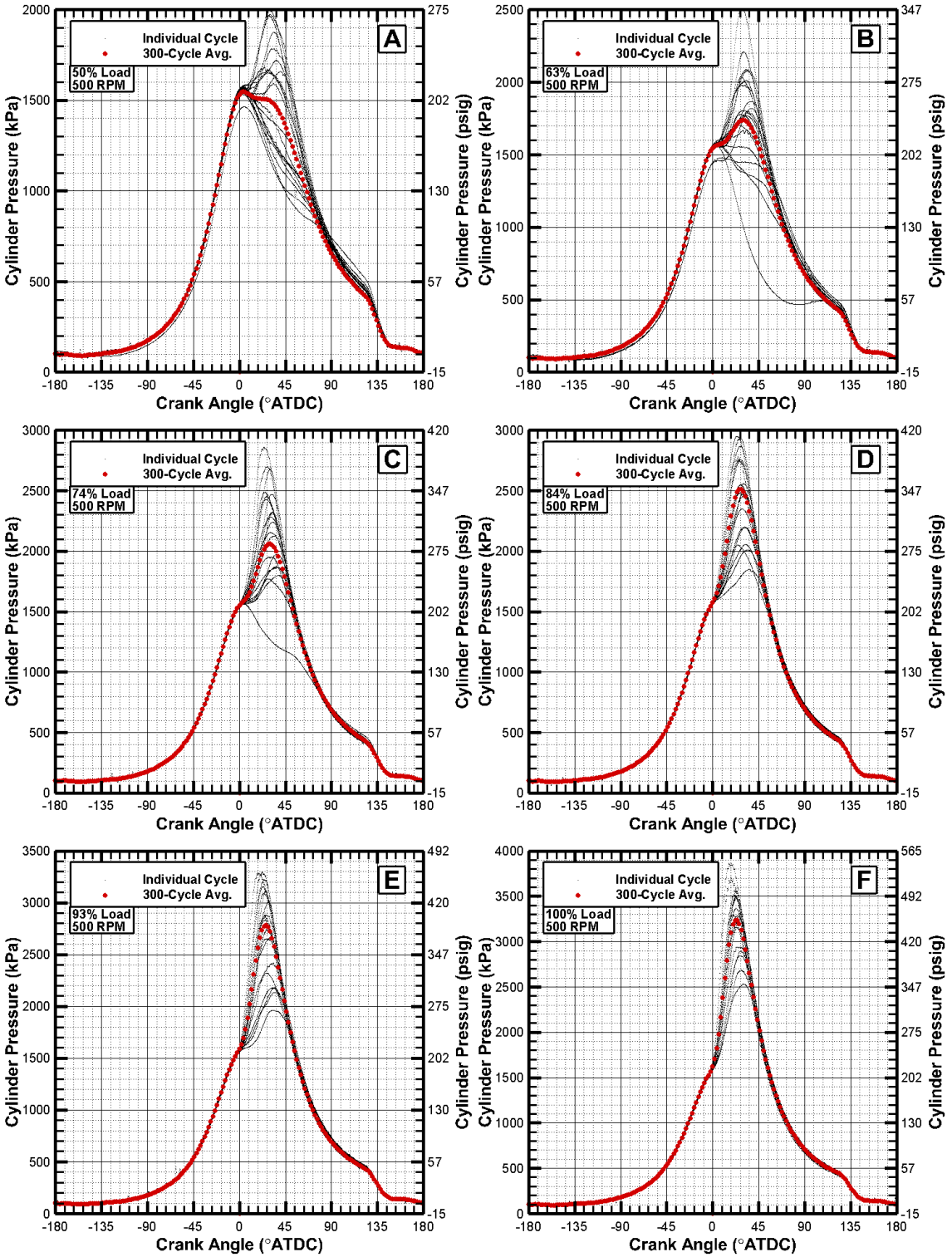

Figure B- 7. Twenty non-sequential individual cycles and 300-cycle averaged in-cylinder pressure measurements are shown as a function of crank angle at 500 RPM for A) 50% load, B) 63% load, C) 74% load, D) 84% load, E) 93% load, and F) 100% load.

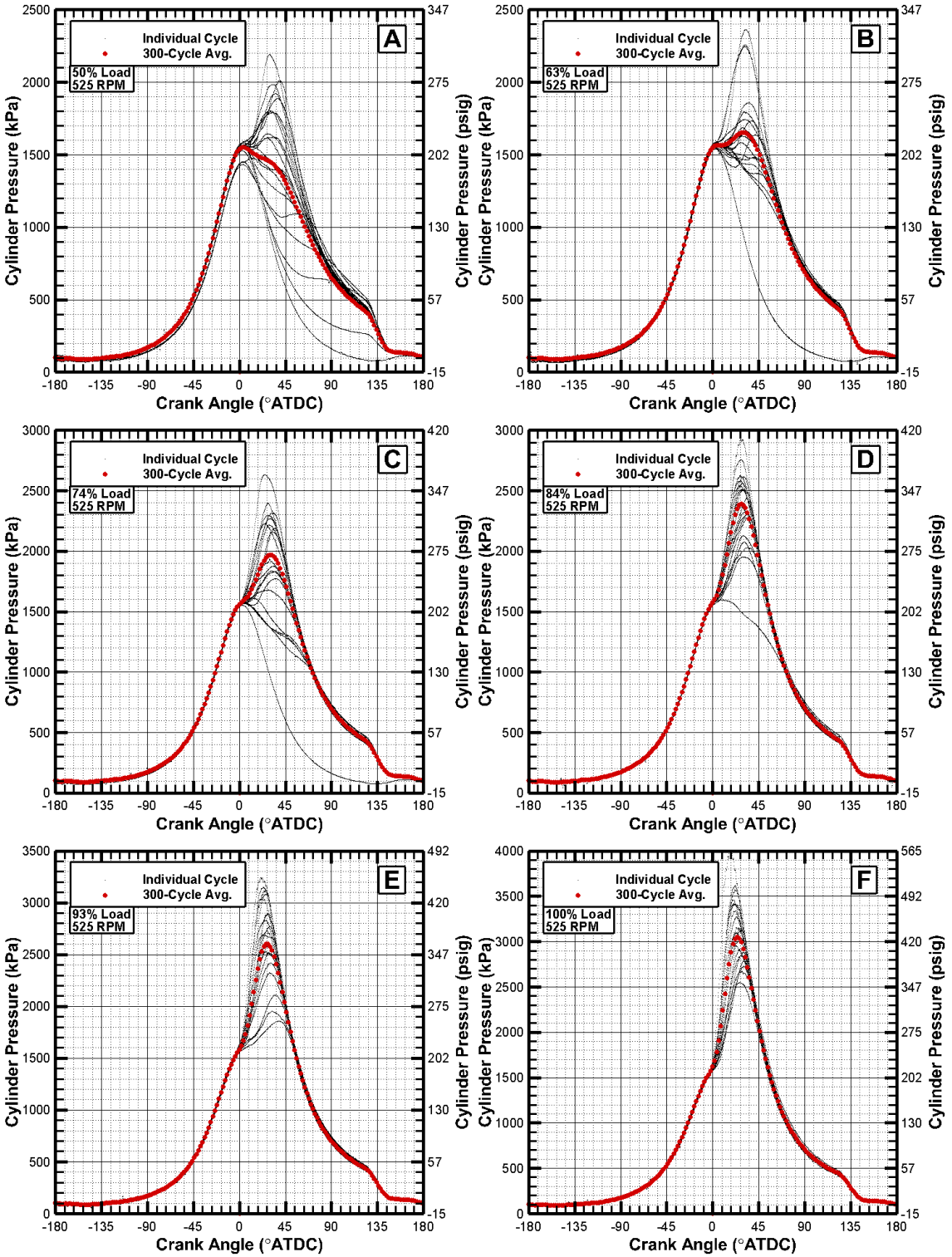

Figure B- 8. Twenty non-sequential individual cycles and 300-cycle averaged in-cylinder pressure measurements are shown as a function of crank angle at 525 RPM for A) 50% load, B) 63% load, C) 74% load, D) 84% load, E) 93% load, and F) 100% load.

APPENDIX C

SCAVENGING EFFICIENCY RESULTS

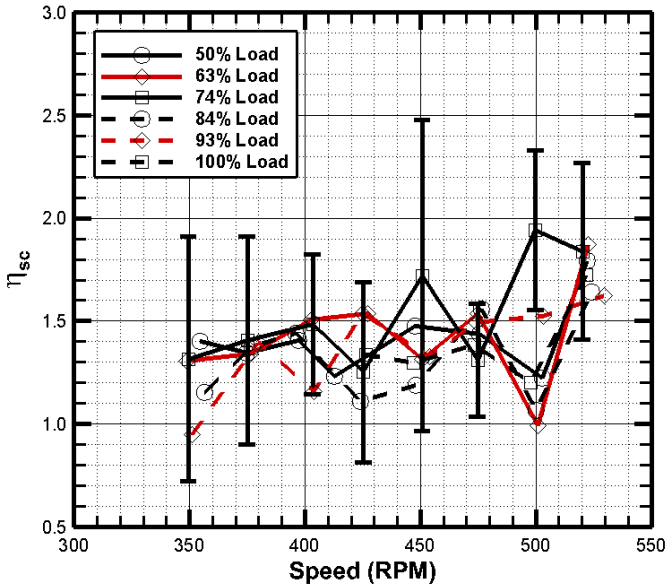

Figure C- 1. The scavenging efficiency as a function of engine speed and load with error bars shown on the 74% dataset representing 95% confidence intervals.